Advanced all-fiber optofluidic devices

SEBASTIÁN ETCHEVERRY CABRERA

Stockholm 2017

Doctoral Thesis
Department of Applied Physics
KTH - Royal Institute of Technology

Advanced all-fiber optofluidic devices

Laser Physics
Department of Applied Physics
KTH – Royal Institute of Technology
106 91 Stockholm

ISBN: 978-91-7729-572-3
TRITA-FYS 2017:65
ISSN 0280-316X
ISRN KTH/FYS/–17:65—SE

Akademisk avhandling som med tillstånd av Kungliga Tekniska Högskolan framlägges till offentlig granskning för avläggande av teknologie doktorsexamen fredagen den 14 november 2017 kl. 13.00 i sal FB42, Albanova, Roslagstullsbacken 21, KTH, Stockholm. Avhandlingen kommer att försvaras på engelska.

Cover picture: Microscope images of the integrated detection micro-chamber of the fiber flow cytometer presented in paper III. (left) lateral and (right) cross-sectional views of the micro-chamber.

Printed by Universitetsservice US AB, Stockholm 2017

Abstract

Significant technological advances of the last years have been possible by developments in Optofluidics, which is a field that deals with the integration of optics and microfluidics into single devices.

The work described in this thesis is based on five scientific publications related to the use of fiber optic technology to build integrated optofluidic devices. The first three publications are within the field of life-science and point towards in-vivo and point-of-care applications, whereas the last two publications cover the study and the use of plasmonic nanoparticles for electrical modulation of light.

Aiming at developing useful tools for in-vivo biological applications, the first publication consists of designing and testing a functional optical fiber for real-time monitoring and selective collection of fluorescent microparticles. This probe relies on a microstructured optical fiber with a hole along its cladding, which is used to selectively aspirate individual particles of interest once their fluorescence signal is detected. On the same line of research, the second publication contemplates the fabrication of a fiber probe that traps single microparticles and allows for remote detection of their optical properties. This probe is also based on a microstructured fiber that enables particle trapping by fluidic forces. The third publication addresses the development of an all-fiber miniaturized flow cytometer for point-of-care applications. This system can analyze, with excellent accuracy and sensitivity, up to 2500 cells per second by measuring their fluorescence and scattering signal. A novel microfluidic technique, called Elasto-inertial microfluidics, is employed for aligning the cells into a single-stream to optimize detection and throughput.

The fourth publication involves the experimental and theoretical study of the electrical-induced alignment of plasmonic gold nanorods in suspension and its applicability to control light transmission. This study is done by using an all-fiber optofluidic device, based on a liquid-core fiber, which facilitates the interaction of light, electric fields, and liquid suspensions. Results show that nanorods can be aligned in microseconds, providing a much better performance than liquid-crystal devices. Finally, the fifth publication consists of an upgrade of the previous device by integrating four electrodes in the cladding of the liquid-core fiber. This improvement enables nanosecond response time and the possibility of digitally switching nanorods between two orthogonal aligned states, overcoming the limitation of slow thermal relaxation.

The work presented here shows that optofluidics based on optical fibers is a robust and convenient platform, as well as a promising direction for the developing of novel instruments in fields such as life-science, non-linear optics, plasmonic, and sensing.

Sammanfattning

Stora framsteg har under senare år gjorts inom optofluidik, vilket är området som kombinerar optik och mikrofluidik i integrerad komponenter.

Denna avhandling baseras på fem vetenskapliga tidskriftsartiklar där avancerad fiberoptisk teknologi använts för att konstruera integrerade optofluidiska komponenter. I de tre första artiklarna beskrivs komponenter som kan användas inom livsvetenskaperna, med potential för in vivo- och point of care-tillämpningar, medan de sista två artiklarna behandlar hur man kan styra plasmoniska nanostavar i fibrer elektriskt, och dess användning för att modulera ljus.

I den första artikeln har en funktionell fiberoptisk prob designats för realtidsövervakning och selektiv infångning av fluorescerande mikropartiklar som ett steg i att utveckla användbara verktyg för biologiska in vivo-tillämpningar. Proben bygger på en mikrostrukturerad optisk fiber med längsgående hål i manteln. Den används för att fånga in mikrometerstora partiklar från en lösning när de detekterats via fluorescens. I en uppföljningsartikel har vi använt en liknande fiberoptisk prob för att fånga in och analysera enskilda mikropartiklar och bestämma deras egenskaper optiskt. Här utnyttjades hydrodynamiska egenskaper i fibrerna för att få en kraftfull detektion. Den tredje artikeln handlar om en miniatyriserad flödescytometer baserad på samma typ av optisk fiber. Med denna har vi med hög känslighet och noggrannhet kunnat analysera upp till 2500 celler per sekund genom att mäta deras fluorescens och spridningssignatur. Här har vi också utnyttjat s.k. elasto inert-mikrofluidik, för att upplinjera cellerna i en fokuserad ström och därmed uppnå optimerad detektion och flödeshastighet.

Den fjärde artikeln beskriver teoretiska och experimentella studier av plasmoniska nanostavar i lösning i en vätskekärnefiber. Nanostavarna upplinjerades med hjälp av elektriska fält applicerade på elektroder integrerade på en cell som kopplats till fibern. Detta utnyttjades för att kontrollera transmissionen i fibern. Kombinationen av ljus och stavarna i lösning med de integrerade elektroderna ger en mycket kompakt och robust lösning på upplinjeringsproblematiken och de små dimensionerna innebär att endast låga spänningar behövs. Komponenten reagerar på mikrosekundskalan och har väsentligt bättre prestanda än traditionella vätskekristallmodulatorer. Den femte artikeln, slutligen, handlar om en förbättrad variant av föregående komponent där fyra elektroder har integrerats i manteln på fibern för upplinjering av nanostavarna i vätskekärnfibern. Nu erhölls switchtider på nanosekunder och vi kunde få digital switchning mellan två ortogonala tillstånd och därmed kringgå begränsningen i föregående experiment som orsakades av den långsamma termiska relaxationen av nanostavarna när fältet var avslaget.

Arbetet som presenterats här visar att optiska fiber är en robust plattform för optofluidik och det är ett lovande första steg mot instrumentering inom områden som icke-linjär optik, plasmonik, mätteknik, övervakning och inom livsvetenskap.

Publications included in this thesis

This thesis is based on the following journal papers.

I. A. Sudirman, **S. Etcheverry**, M. Stjernström, F. Laurell, and W. Margulis, "A fiber optic system for detection and collection of micrometer-size particles," *Optics Express* 22, 21480-21487 (2014).

II. **S. Etcheverry**, A. Russom, F. Laurell, and W. Margulis, "Fluidic trapping and optical detection of microparticles with a functional optical fiber," *Submitted*.

III. **S. Etcheverry**, A. Faridi, H. Ramachandraiah, T. Kumar, W. Margulis, F. Laurell, and A. Russom, "High performance micro-flow cytometer based on optical fibre," *Scientific Reports* 7, 5628 (2017).

IV. **S. Etcheverry**, L. F. Araujo, G. K. B. da Costa, J. M. B. Pereira, A. R. Camara, J. Naciri, B. R. Ratna, I. Hernández-Romano, C. J. S. de Matos, I. C. S. Carvalho, W. Margulis, and J. Fontana, "Microsecond switching of plasmonic nanorods in an all-fiber optofluidic component," *Optica* 4, 864-870 (2017).

V. **S. Etcheverry**, L. F. Araujo, I. C. S. Carvalho, W. Margulis, and Jake Fontana, "Digital switching of plasmonic nanorods with nanosecond response times," *Submitted.*

Description of author contributions

- **Paper I**
  I performed final experiments to demonstrate the proposed system.
- **Paper II**
  I designed the fiber component and conducted experiments assisted by my co-supervisor Walter Margulis. I prepared the figures and contributed to writing the manuscript.
- **Paper III**
  I took part in designing the fiber component and the experiments. I fabricated the components and the optical system with the assistance of Walter Margulis, Fredrik Laurell, and Aman Russom. I performed the experiments and the data analysis with the assistance of A. Faridi, H. Ramachandraiah, and T. Kumar. I prepared the figures and contributed to writing the manuscript.
- **Paper IV**
  I took part in designing the fiber component and the experiments. I fabricated the fiber components and performed the experiments with the assistance of my co-supervisor Walter Margulis. I took part in developing the theoretical model and numerical simulations. I prepared the figures and contributed to writing the manuscript.
- **Paper V**
  I participated in designing the experiments. I fabricated the components and performed the experiments with the assistance of my co-supervisor Walter Margulis. I prepared the figures and contributed to writing the manuscript.

Author's publications not included in this thesis

- G. S. Lobov, A. Marinins, S. Etcheverry, Y. Chao, E. Vasileva, A. Sugunan, F. Laurell, L. Thylén, L. Wosinski, M. Östling, M. S. Toprak, and S. Popov, "Direct birefringence and transmission modulation via dynamic alignment of P3HT nanofibers in an advanced opto-fluidic component," *Optical Material Express* 7, 52–61 (2017).
- D. Goyeneche, G. Cañas, S. Etcheverry, E. S. Gómez, G. B. Xavier, G. Lima, and A. Delgado, "Five Measurement Bases Determine Pure Quantum States on Any Dimension," *Physical Review Letters* 115, 090401 (2015).
- R. Allio, D. Guzmán-Silva, C. Cantillano, L. Morales-Inostroza, D. Lopez-Gonzalez, S. Etcheverry, R. A. Vicencio, and J. Armijo, "Photorefractive writing and probing of anisotropic linear and nonlinear lattices," *Journal of Optics* 17, 025101 (2015).
- G. Cañas, M. Arias, S. Etcheverry, E. S. Gómez, A. Cabello, G. B. Xavier, and G. Lima, "Applying the simplest Kochen-Specker set for quantum information processing," *Physical Review Letters* 113, 090404 (2014).
- G. Cañas, S. Etcheverry, E. S. Gómez, C. Saavedra, G. B. Xavier, G. Lima, and A. Cabello, "Experimental implementation of an eight-dimensional Kochen-Specker set and observation of its connection with the Greenberger-Horne-Zeilinger theorem," *Physical Review A* 90, 012119 (2014).
- S. Etcheverry, G. Cañas, E. S. Gómez, W. A. T. Nogueira, C. Saavedra, G. B. Xavier, and G. Lima, "Automated BB84 quantum key distribution session with 16-dimensional states," *Scientific Reports* 3, 2316 (2013).
- A. Arias, S. Etcheverry, P. Solano, J. P. Staforelli, M. J. Gallardo, H.Rubinstein-Dunlop, and C. Saavedra, "Rotation and orientation control of birefringent microparticles in holographic optical tweezers," *Optics Express* 21, 102-111 (2013), highlighted in *Virtual Journal for Biomedical Optics*.
- S. Etcheverry, M. J. Gallardo, P. Solano, M. Suwalsky, O. Mesquita, and C. Saavedra, "Real time study of shape and thermal fluctuations in the echinocyte transformation of human erythrocytes using Defocusing Microscopy," *Journal of Biomedical Optics* 17(10), 106013 (2012).

Conference presentations

- L. F. Araujo, S. Etcheverry, J. M. Pereira, W. Margulis, J. Fontana, I. Carvalho, "In-fiber optofluidic alignment of Au-nanorods," *WSOF 2017*, Limassol, Cyprus, oral presentation (October 2017).
- S. Etcheverry, A. Faridi, H. Ramachandraiah, W. Margulis, F. Laurell, and A. Russom, "All fiber based micro-flow cytometer by combining optical fiber with inertial focusing," *MicroTAS 2017*, Dublin, Ireland, poster presentation (October 2016).
- L. F. Araujo, S. Etcheverry, G. K. Costa, J. M. B. Pereira, A. R. Camara, C. J. De Matos, W. Margulis, J. Fontana, I. C. Carvalho, "Photonics with Special Optical Fibers and Nanoparticles," *LAOP 2016*, Medellin, Colombia, oral presentation (August 2016).
- S. Etcheverry, A. Faridi, H. Ramachandraiah, W. Margulis, F. Laurell, and A. Russom, "Optofludics in microstructured fibers combining particle elasto-inertial focusing and fluorescence," *CLEO 2016*, San Jose, USA, oral presentation (June 2016).
- S. Etcheverry, A. Faridi, H. Ramachandraiah, W. Margulis, A. Russom, and F. Laurell. "A microstructured optical fiber for optofluidics," *MSW 2016*, Lund, Sweden, poster presentation (May 2016).
- S. Etcheverry, A. Sudirman, W. Margulis, and F. Laurell, "Identification and collection of particles with optical fibers," *ECBO 2015*, Munich, Germany, oral presentation (June 2015).
- S. Etcheverry, A. Sudirman, F. Laurell, and W. Margulis, "Identification and retrieval of particles with microstructured optical Fibers," *LAOP 2014*, Cancun, Mexico, oral presentation (November 2014).

Acknowledgements

First of all, I would like to express my gratitude to my supervisors; Water Margulis for all the ideas, discussions, and for always taking the time to talk about the problems I was encountering in the lab and coming up with solutions. Fredrik Laurell, for accepting me as a member of your group and for the continuous support that made it possible to conduct this research. I could not have imagined having better supervisors. I learned a lot from both of you.

Besides my supervisors, I would like to thank the collaborators I had during my Ph.D., without whom the present work would not have been possible; Aman Russom and his group for the splendid time working together. Aman, it was a pleasure to go to your lab and learn more about cells and microfluidics. Jake Fontana and Isabel Carvalho for the fruitful collaboration. Thank you, Jake, for pushing the finalization of the papers and proofreading part of this thesis, and Isabel, for your hospitality during my stay in Rio de Janeiro. Also, I would like to thank Christiano de Matos and his group for the kind treatment I received during my visit to his lab in São Paulo.

I would like to thank all my co-workers at RISE Acreo for helping me whenever I needed something and for making Acreo such a great place to work. My special gratitude to Oleksandr Tarasenko for sharing his technical knowledge and Leif Kjellberg for his assistance with electronics. I thank my fellows at KTH Laser physics for the moments spent every time I went to Albanova and for making me feel part of the group. I also thank Sergei Popov and his group, as well as the people that work at SICS and HST-Lab Acreo for all the coffee breaks and lunches together.

I would like to express my warm thanks to the friends I made during these four years in Sweden. Especially Juliana, Antonis, Elena, Cristine, Edoardo, Jesus, Marta, Matteo, Chiara, Alex, Carol, Riaan, Robert, and Beatriz for all the good times and laughs that made me feel happy even during stressful periods. Finally, I would like to thank my family and friends in Chile for always being there for me despite the distance. In particular, Carolina for all the support when I decided to move to Sweden, and my mother Dina Cabrera for her unconditional love and care.

The work presented in this thesis was supported by the Swedish Research Council, the Linnaeus Centre ADOPT, and the Knut and Alice Wallenberg Foundation. I also gratefully acknowledge a scholarship from CONICYT Chile for pursuing doctoral studies.

Contents

Chapter 1

Introduction

The work presented in this thesis is based on the development of advanced all-fiber optofluidic devices for life-science and plasmonics applications. This introductory section gives a brief review of the fields explored in this work; fiber optics, microfluidics, optofludics, and plasmonics. Subsequently, an introduction to lab-on-a-fiber and all-fiber optofluidic devices is presented. This section ends with an overview of the present thesis.

1.1 Fiber optics

Over the last four decades, optical fibers have become one of the most fundamental parts of telecommunication and have enabled a tremendous growth of data transmission capability [1]. Optical fibers are low-loss cylindrical waveguides typically composed of a germanium doped-silica core surrounded by a silica cladding. The germanium slightly increases the refractive index of the core, allowing the light to be confined and guided by total internal reflection [2, 3]. Optical fibers are flexible, transparent, low-cost, suitable for harsh environments, and capable of guiding light to and from areas which may be difficult to access. These properties have stimulated the use of fibers in different areas beyond communications, such as sensing [4], laser technology [5] and life-science [6]. Sensing technologies have made use of optical fibers for a vast variety of applications involving acoustic, temperature, pressure and strain monitoring [4, 7]. Currently, Fiber optic sensors (FOS) are a well-established market providing measuring tools which are routinely used in the industry. Furthermore, the fact that an optical fiber guides light with low-loss in a controlled medium enables its use in the field of high-power lasers and amplifiers [8]. For instance, stimulated emission can be obtained by doping the silica core with rare-earth ions, which serve as the gain medium for laser action [9]. The field of life-science has also exploited fiber optics to build less invasive instruments for detecting and treating diseases. An example of this is the endoscope, a device which provides imaging inside the human body [10, 11]. Optical coherence tomog-

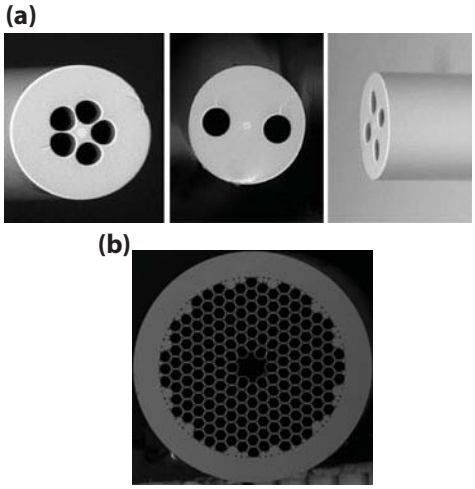

Figure 1.1: Microstructured optical fibers. (a) Fibers with holes along the cladding. (b) Hollow-core photonic crystal fiber.

raphy (OCT), a technique that uses low-coherence interferometry to obtain three-dimensional images of objects, has incorporated optical fibers to perform analysis of biological tissues and organisms [12]. Aiming at developing novel technologies, different microstructured optical fibers have been manufactured [13, 14], Fig. 1.1. For instance, two holes along the fiber cladding, Fig. 1.1(a, center), provide the possibility of inserting metal into these holes and applying an electric field across the core for applications such as second-harmonic generation and electro-optical modulation [15]. Photonic crystal fibers (PCFs) are a type of microstructured optical fiber that possesses a periodic structure and allow for light confinement by photonic bandgap effects. This enable the guidance of light in a hollow core surrounded by a microstructured silica cladding (i.e. hollow-core PCF), Fig. 1.1(b), resulting in a favorable platform for high-power transmission, non-linear optics, and highly sensitive sensors [16].

1.2 Microfluidics and optofluidics

Microfluidics is a research field that deals with the physics and control of fluids in channels of micrometer dimensions [17, 18]. Fluids in microchannels behave differently than in channels of larger size. Capillary forces and surface tension are dominant, while the effect of gravity is less relevant [19, 20]. The precise manipulation of small fluid volumes provided by microfluidics techniques is particularly important for life-science applications, where the amount of sample is limited and the objects of interest, such as cells or bacteria, have dimensions that are comparable to the ones of the channel [21]. Microfluidic technology allows, for instance, controlled mixing of fluids [22], cell separation [23], and cell trapping [24]. The microfluidic platform has exploited optics by using external microscopes, embedded

optical fibers, or waveguides to perform detection and analysis of bioparticles [25], among other applications. The integration of optics and microfluidics has given rise to the field of Optofluidics [25–28]. Applications found within Optofluidics include dye lasers [29], active control and focusing of light [30, 31], optofluidics microscopy [32], particle transport and trapping by light [33], and laser-induced microdroplets [34, 35].

The field of Lab-on-a-chip (LOC) employs microfluidics and optofluidics as part of its toolkit to integrate into a single microchip the instruments and processes used in the medical laboratory [36, 37]. Currently, LOC is demonstrating its potential, providing micro-systems that are low-cost, portable, efficient, and robust. These properties make LOC systems suitable for point-of-care diagnosis (i. e. immediate diagnostics at the patient's location) and a viable replacement for expensive large-scale instruments [38, 39].

1.3 Plasmonics

Plasmonic is a field that studies the interaction of light with metallic particles and structures at the nanoscale [40]. Light impinging on a metal nanoparticle causes collective oscillation of the electron cloud located at the interface between the metal and the non-conductive medium. When the frequency of the light matches the frequency of the oscillation of the electron cloud, resonant light absorption takes place. This phenomenon is known as Localized surface plasmon resonance (Localized SPR) [41, 42]. The absorption spectrum of the light depends on the size, shape, and material of the nanoparticle, as well as the medium refractive index. Localized SPR has been exploited for developing sensors that allow for high resolution and real-time detection of biomolecules [43]. These biosensors rely on the fact that a molecule in contact with the nanoparticle changes the local refractive index and causes a shift in the absorption peak related to the surface plasmon resonance, which can be readily detected. Another application within the field of plasmonics is Surface enhanced raman spectroscopy (SERS), which is a technique capable of detecting single molecules by increasing the Raman scattering in orders of magnitudes using metal nanostructures [44].

1.4 Lab-on-a-fiber

The numerous developments in optical fibers and processing techniques have resulted in the surge of a field called Lab-on-a-fiber (LOF) [45, 46] which mostly focuses on life-science applications, analogously to lab-on-a-chip technologies. LOF is a rapidly emerging field whose main goal is to increase the functionalities of optical fibers to perform multiple and advanced tasks. For instance, LOF deals

with the fabrication of functional fiber probes that can bring the capabilities of lab-on-a-chip technologies for the analysis bio-samples to in-vivo applications. In the future, this could allow performing real-time diagnosis and treatment of diseases by inserting advanced fibers inside the human body. Although the LOF field is at its beginning, many innovative ideas and devices have been demonstrated. For example, fiber-tips with metallic nanostructures that allows for biosensing applications with SERS [47, 48], fibers probes for near-field imaging [49], and fiber-based optical tweezers for single-cell trapping [50, 51]. Part of the work presented in this thesis involves the development of optical fiber probes that allow for selective trapping, isolation or collection of cells. These functional fibers represent a novel tool for in-vivo studies, which could potentially avoid the need for invasive biopsy for identifies diseases [51, 52].

1.5 All-fiber optofluidic devices

Microfluidics chips are typically made of polymer materials such as PDMS [53, 54]. These materials are easy to mold, inexpensive, bio-compatible and transparent, resulting in a good platform for the manipulation and visualization of cells in fluids. However, they have some limitation such as softness and high elasticity that makes them deformable under high-pressure. Besides, they are gas permeable, which despite being favorable for cell culturing, makes the control of fluid evaporation troublesome [55, 56]. Additionally, polymer chips can absorb hydrophobic molecules from solution, are incompatible with several organic solvents, present difficulties for the deposition of metals and dielectrics, and their auto-fluorescence can increase the noise in optical detection schemes [57]. These limitations can be overcome by using glass substrates instead of PDMS. Silica glass is chemically inert, has excellent optical characteristics, has low auto-fluorescence and maintains its shape under high-pressure [58]. However, the fabrication of silica microchips requires expensive instrumentation and clean-room facilities [59]. A low-cost and convenient way of benefiting from the intrinsic advantages of silica for optofluidics is by exploiting optical fiber technology. Silica optical fiber and capillaries are fabricated in kilometer lengths and at a low-cost [60]. They can be assembled using equipment developed for telecommunications to build optofluidic components [26, 61]. This all-fiber optofluidic platform, besides facilitating the integration of light and fluidics, could considerably extend the capabilities of planar microchips by exploiting developments in microstructured optical fibers and photonic crystal fibers. Examples of all-fiber optofluidics devices include high repetition fiber dye lasers [62], liquid-filled PCFs for studying nonlinear propagation of light in solvents [63, 64], and fluidic components based on microstructured fibers for chemical sensing and absorption spectroscopy [65, 66].

The all-fiber optofluidic platform is versatile and can incorporate developments in microfluidics and lab-on-a-chip to contribute to the miniaturization and

cost reduction of medical instruments for point-of-care applications. Part of the work presented in this thesis involves the fabrication of an all-fiber miniaturized flow cytometer [67, 68]. Flow cytometers are devices that enable health disorder identification by performing high-throughput analysis of individual cells. Conventional cytometers are expensive, bulky, difficult to operate, and, therefore, unsuitable for point-of-care. Furthermore, the all-fiber optofluidics platform could be used to build systems based on liquid-core fibers that enable long-distance interaction between light and particles suspended in liquid medium. In this thesis, we present an all-fiber system that allows studying and controlling the optical absorption of a liquid suspension of plasmonic nanorods. Such studies could allow for the development of light modulators and tunable optical elements.

1.6 Overview of this thesis

In general, Lab-on-a-fiber focuses on increasing the functionalities of a single optical fiber, whereas the all-fiber optofluidic platform combines different types of optical fibers and capillaries to build advanced devices for specific applications. The work presented in this thesis is based on five papers, **Papers I-V**, which correspond to applications of lab-on-a-fiber and all-fiber optofluidic technologies. In the context of Lab-on-a-fiber, two advanced fiber probes are presented; In **Paper I** we report a fiber probe that can selectively collect single microparticles based on their fluorescent signal, and in **Paper II** we demonstrate a fiber probe that can trap individual microparticles and allows measuring their optical properties. In the context of all-fiber optofluidic devices; **Paper III** describes a high-performance microflow cytometer entirely built by combining optical fibers and capillaries. This system uses a novel microfluidic technique called Elasto-inertial microfluidics to align particles and cells before detection to guarantee accurate and high-throughput detection. In **Paper IV** we report an all-fiber optofluidic device that allows for the interaction between light, liquid and electric field. We use this tool to study the optical response of a plasmonic nanorods suspension aligned by an external electric field. This paper provides a compelling description of the dynamics of plasmonic nanorods by experimental and theoretical studies. Finally, **Paper V** describes a significant technical improvement of the component presented in the previous paper that allows for fast bi-directional switching of nanorods.

Chapter 1 introduces the fields explored in this thesis and motivates the present work. Chapter 2 describes the theoretical background to deepen the understanding of **Papers I-V**. Chapter 3 summarizes **Papers I-V**, highlighting the motivation of each work. Chapter 4 presents the conclusions of this thesis and possible directions for future work. Finally, the processes and instruments used, as well as the electronic circuits developed are found in the Appendex. **Papers I-V** are reprinted in the end of this thesis.

Chapter 2

Theoretical background

2.1 Optical fibers

In **Papers I**, **II** and **III**, we used optical fibers to excite fluorescence microparticles and collect their emitted light. In this section, we present a theoretical background for the problem of particle excitation and light collection by single optical fiber.

2.1.1 Optical fibers: basic definitions

As mention in the introduction, optical fibers are typically composed of a germanium oxide doped-silica core with higher refractive index surrounded by a silica cladding with lower refractive index, allowing for light guidance by total internal reflection [3]. The numerical aperture NA of a optical fiber is defined as

$$NA = \sqrt{n_{core}^2 - n_{clad}^2}, \tag{2.1}$$

where n_{core} and n_{clad} are the refractive index of the core and cladding, respectively. As shown in Fig. 2.1, the numerical aperture characterizes the maximum angle θ_{max} of an incident ray that can be coupled and guided in the fiber,

$$NA = n_i \sin \theta_{max} \tag{2.2}$$

The parameter n_i is the refractive index of medium outside the fiber. A standard single-mode optical fiber for telecommunications (SMF-28) has a numerical aperture $NA = 0.14$ at a light wavelength of $\lambda = 1310$ nm, a core refractive index of $n_{core} = 1.4475$, and a cladding refractive index of $n_{clad} = 1.444$. The core diameter d_{core} and the cladding diameter d_{clad} are typically 9 µm and 125 µm, respectively.

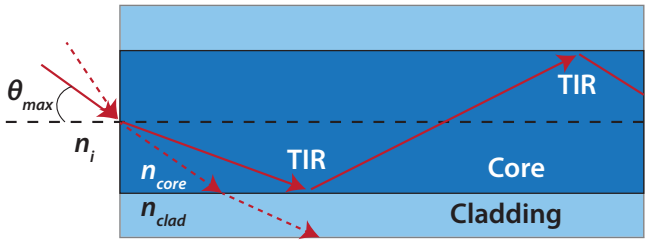

Figure 2.1: Optical fiber: Maximum acceptance angle.

2.1.2 Particle excitation and light collection

A light beam spreading out from an optical fiber of core diameter d_{core} has an approximate Gaussian intensity profile $I(r,z)$ given by [3]

$$I(r,z) = \frac{2P}{\pi w(z)^2} \exp\left(\frac{-2r^2}{w(z)^2}\right), \tag{2.3}$$

where P is the total laser power and $w(z)$ is the spot spatial distribition determined by

$$w(z) = w_0 \sqrt{1 + \left(\frac{z}{z_R}\right)^2} \tag{2.4}$$

The parameter z_R is called Rayleigh range and is defined as $z_R = w_0^2 n_i/\lambda$, where $w_0 = MFD/2$ is the waist size. MFD is the mode field diameter of the fiber and is typically slightly larger than the core diameter due to the fraction of the light guided in the cladding. For instance, in standard telecoms fiber $d_{core} = 9$ µm and $MFD \approx 10.4$ µm for $\lambda = 1310$ nm. The Rayleigh range is the distance from the axial position of the fiber waist ($z = 0$) to the position where the spot size is $\sqrt{2}w_0$, as illustrated in Fig. 2.2(a). Fig. 2.2(b) shows a simulation, obtained from Eq. 2.3, of a Gaussian beam spreading out an optical fiber of $MFD \approx 10$ µm. The intensity distribution shown in Fig. 2.2(b) describes the excitation signal available for optically pumping fluorescent microparticles. The exicitation light is maximum for particles located near the fiber end-face and aligned with the fiber core.

In the schemes used in **Papers I-III**, a single optical fiber carries the excitation light towards the particles and collects the emitted light, which is guided back toward a detection system. To estimate the efficiency of light collection by an optical fiber, we used a theoretical approach based on the reference [69], *"Enhanced fluorescence signal in nonlinear microscopy through supplementary fiber-optic light collection"*.

Consider a point-source emitting light in all directions which is located at an axial distance z and a radial distance r from the fiber-end, as illustrated in the Fig. 2.3(a). The amount of light that reaches the core of the optical fiber is defined

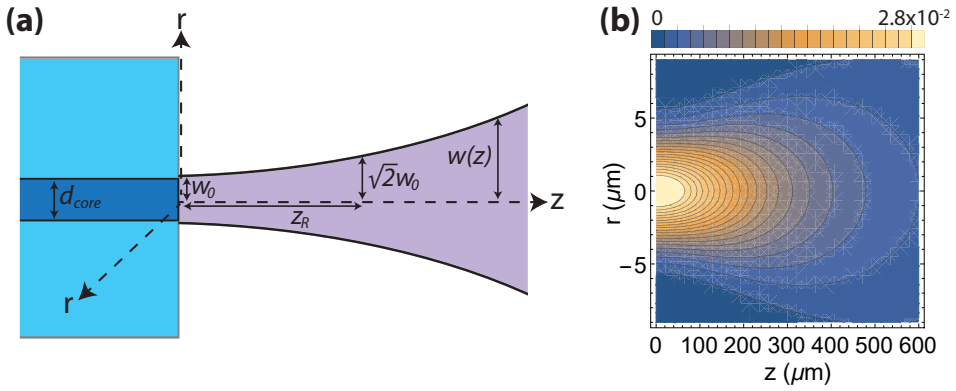

Figure 2.2: Schematic of Gaussian beam spreading out from an optical fiber. (b) Bi-dimensional map of Eq. 2.3 illustrating the divergence of a Gaussian beam exiting an optical fiber. Parameters used are: $MFD = 10$ µm, $n_i = 1.33$, $\lambda = 450$ nm and $P = 1$.

by the solid angle $\Omega_f(r, z)$,

$$\Omega_f(r, z) = 2\pi \left[1 - \cos\left(\tan^{-1}\left(\frac{d_{core}}{2z}\cos\gamma^{\frac{3}{2}}\right)\right)\right], \tag{2.5}$$

where $\gamma = \tan^{-1}(r/z)$ is the off-axis angle. The light defined by $\Omega_f(r, z)$ is collected and guided only if it is within the solid angle defined by the fiber numerical aperture, $\Omega_{NA}(r, z)$,

$$\Omega_{NA} = 2\pi \left[1 - \cos\left(\tan^{-1}\left(\frac{NA}{n_i}\right)\right)\right] \tag{2.6}$$

Therefore, the collection efficiency (i.e. fraction collected of the light emitted by the point-source) of the optical fiber $\eta(r, z)$, normalized to 4π, can be obtained from

$$\eta(r, z) = \min\left(\Omega_f(r, z), \Omega_{NA}\right) A/4\pi \tag{2.7}$$

The quantity A corresponds to the area of the region defined by Ω_f at $z = 0$ that overlaps the fiber core, as shown in Fig. 2.3(a), and its calculation reduces to a circle-circle intersection problem [69]. For a point source located at the fiber axis $r = 0$, Fig. 2.3(b), $A = 1$ and Eq. 2.5 simplifies to

$$\Omega_f(z) = 2\pi \left[1 - \cos\left(\tan^{-1}\left(\frac{d_{core}}{2z}\right)\right)\right] \tag{2.8}$$

If the point-source is near the fiber-end, the collection efficiency is constant and limited by Ω_{NA}, Fig. 2.3(b). This means that light rays impinging the fiber core at incidence angles larger than the acceptance angle θ_{max} (Eq. 2.2) are not confined and therefore lost, as illustrated in Fig. 2.1. On the other hand, if the point-source is far from the fiber-end, the collection efficiency is limited by $\Omega_f(z)$, Fig. 2.3(c), and its

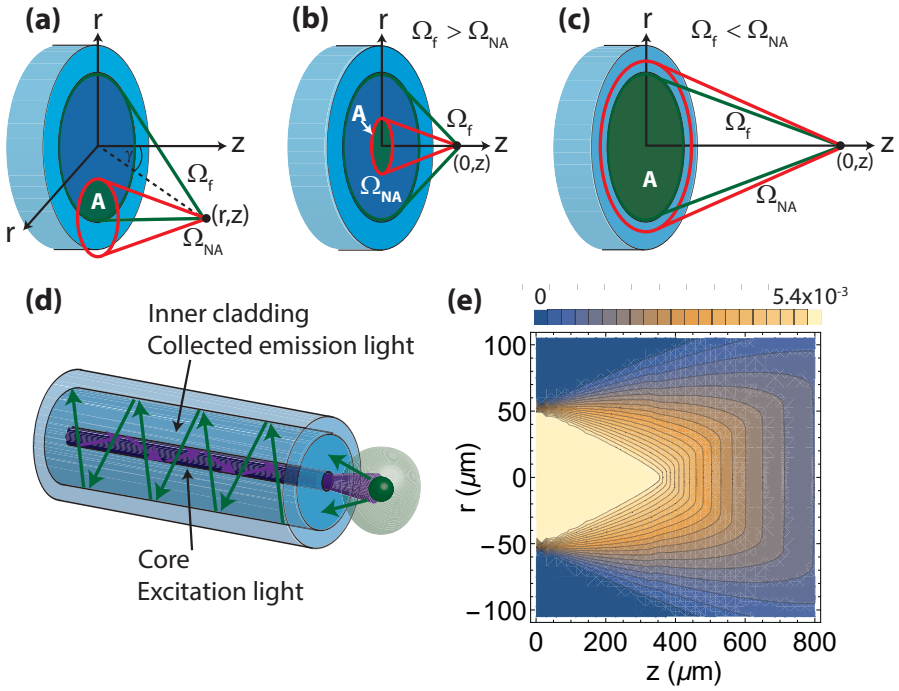

Figure 2.3: (a) Solid angle defined by a point-source located at (r, z). (b) Point-source located at the fiber axis $(0, z)$ and near the fiber-end, $\Omega_f > \Omega_{NA}$. (c) Point-source located at the fiber axis $(0, z)$ and far from the fiber-end, $\Omega_f < \Omega_{NA}$. The red cone illustrates the solid angle defined by the numerical aperture Ω_{NA}, within which rays are guided. The green cone illustrates the maximum illuminated solid angle on the core at the fiber-end, Ω_f. (d) Detection scheme based on a double-clad optical fiber. (e) Bi-dimensional map of the collection efficiency $\eta(r, z)$ for a fiber with $d_{core} = 105$ µm and $NA = 0.2$. Figures (e) and (d) correspond to the system presented **in Paper III**

value decreases with z. In this case, all the light rays reaching the fiber core have an incidence angle smaller than θ_{max} and, hence, the light collection efficiency is only restricted by the size of the fiber core. For instance, in **Paper III**, we used a double-clad fiber that allows for particle excitation with light guided in a small core and for light collection by a larger inner cladding, as shown in Fig. 2.3(c). The diameter of the inner cladding is 105 µm, and its numerical aperture 0.2. Considering these parameters and applying $d_{core} = 105$ µm in Eq. 2.5, a bi-dimensional map of the collection efficiency, Fig. 2.3(d), is obtained from Eq. 2.7. The collection efficiency is maximum and saturated to 5.4×10^{-3} for a particle located in the region defined by Ω_{NA}, according to Eq. 2.6. This means that 0.54% of the light emitted by the particle is collected. Consequently, approaching an emitting particle along the axis from 300 µm does not increase the fraction of light collected.

The detection schemes of the fiber probes presented **Paper I** and **Paper II** are similar to the one described in **Paper III**. However, they differ in some characteristics regarding the type fiber used. In **Paper I**, the same 8 µm core of optical fiber with $NA = 0.12$ is used for both excitation and light collection, resulting in a maxi-

mum collection efficiency of 0.25% for a particle located at a distance less that $40\,\mu\mathrm{m}$ from the fiber-end. In **Paper II** the collection efficiency is considerably enhanced to 5.4% by using a double-clad configuration with high numerical aperture $NA = 0.6$, made possible by a water cladding surrounding the core of a microstructured optical fiber. **Papers I-III**, reprinted in the end of this thesis, provide a detailed description of these three different schemes, as well as the analysis of their efficiency for particle excitation and light collection.

2.2 Single particle trapping

Paper II describes a functional fiber probe that allow for trapping individual microparticles and measuring their optical properties. This section present a brief review of some of the existing techniques for single particle trapping.

2.2.1 Optical tweezers and micropipette aspiration

The capability of trapping and precisely manipulating particles has been widely used for studying properties of cells and biomolecules [70]. Two of the most common techniques for this purpose are optical tweezers [71] and micropipette aspiration [72].

Optical tweezers allow for non-contact and three-dimensional trapping of dielectric particles. This system is based on a highly-focused Gaussian laser beam obtained using a microscope objective with high numerical aperture, as depicted schematically in Fig. 2.4(a). A particle impinged by the laser beam experiences a gradient force that drives it toward the beam waist, where the electric field is stronger. Besides, a scattering force, originating from conservation of momentum in the interaction between particle and photons, pushes the particle along the beam direction. The balance between these two forces causes the confinement of the particle at a position slightly below the beam waist [73]. Applications of optical tweezers include single cell and bacteria manipulation [74, 75], mechanical studies of bioparticles [74, 76], and quantification of small forces (pico-newton) [77]. An important development in this technique is its extension to holographic optical tweezers, which allows for the trapping and independent control of multiple particles by shaping the phase of the laser beam before focusing [78]. Aiming at miniaturization and increased versatility, fiber-based optical tweezers have been demonstrated by employing tapered optical fibers [50] or microstructured fiber-tips [51], for instance. Such systems could find applications in deep-tissue cell manipulation and in-vivo biological studies.

Micropipette aspiration relies on the simple use of a suction force to trap a particle at the tip of a pipette that has a diameter smaller than the particle, as shown in Fig. 2.4(b). This technique has been used for studying physical properties of

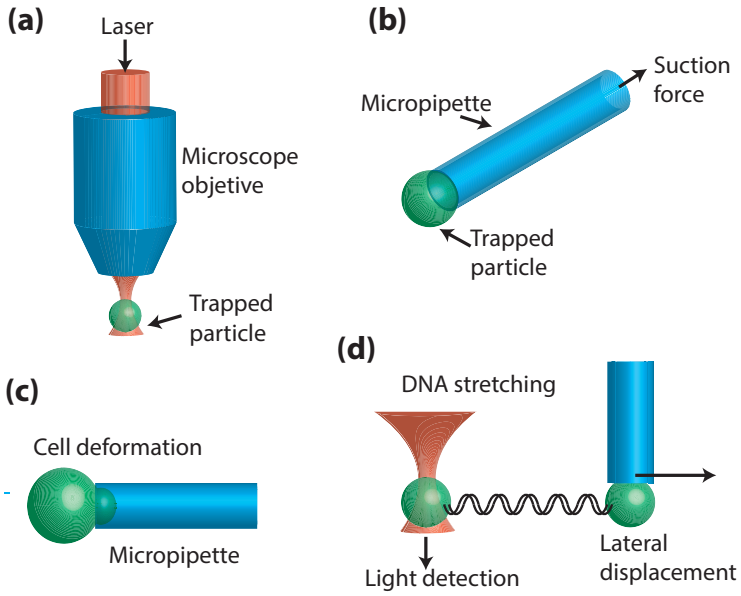

Figure 2.4: Schematic of (a) Optical tweezers, (b) Micropipette aspiration, (c) Deformation studies by using micropipitte aspiration, and (d) DNA streching employing optical tweezers and micropipitte aspiration.

biological membranes since it allows for deforming the cell membrane by extending it into the pipette [70, 72], Fig. 2.4(c). Measuring this deformation, by using an external microscope, enables the retrieval of elastic and viscous parameters of the cell, as well as provides information about its internal structure. For instance, experiments based on micropipette aspiration have significantly contributed to the understanding of how red blood cells deform and flow through tiny vessels [79].

Schemes that combine optical tweezers and micropipette aspiration have led to valuable knowledge about mechanical properties of single DNA molecules [80]. In these experiments, a spherical microparticle trapped by an optical tweezer is attached to one side of a DNA molecule, whereas the other side is attached to a particle trapped by a micropipette, as depicted in Fig. 2.4(d). Lateral displacement of the micropipette trapped-particle stretches the DNA molecule and, at some point, pulls the optically trapped-particle. Precise measurement of this pulling force, carried out by analyzing the light scattered by the particle in the optical tweezer, allows, for instance, estimating elastic properties of the DNA molecule.

The functional fiber probe presented **Paper II** integrates particle trapping using micropipette aspiration with optical analysis. A description of this optical fiber probe can be found in **Paper II**, summarized in Sec. 3.2.

2.3 Flow cytometry

As mentioned in the introduction, a high-performance micro-flow cytometer is reported in **Paper III**. Accordingly, in this section, we present a brief description of flow cytometry and developments that have been made in this field.

2.3.1 Flow cytometers: working principle

Conventional flow cytometers are automated laser-based tools that allow qualitative and quantitative multi-parametric analysis of individual cells [67, 68]. They are routinely used in the medical laboratory and biomedical research for health disorder diagnostics and characterization of cell properties. Fig. 2.5(a) shows a schematic of the working principle of a flow cytometer. They possess a fluidic system that organizes fluorescently labeled cells into a single stream (i. e. cell focusing) utilizing a sheath fluid. Typically, cells are analyzed by targeting them with laser beams while they flow through a detection region, one at a time. The scattered light at different angles and fluorescence emitted by the cells are measured by a system of photomultiplier detectors. The data acquired is processed by a computer software to retrieve parameters related to the properties of cells. Scattering measurements quantify the total number of cells and provide information about cell size, granularity, number of organelles, and membrane complexity. Fluorescence measurements allow differentiating types of cells which have been labeled, for instance, by specific fluorescent antibodies [81]. Modern flow cytometers achieve a

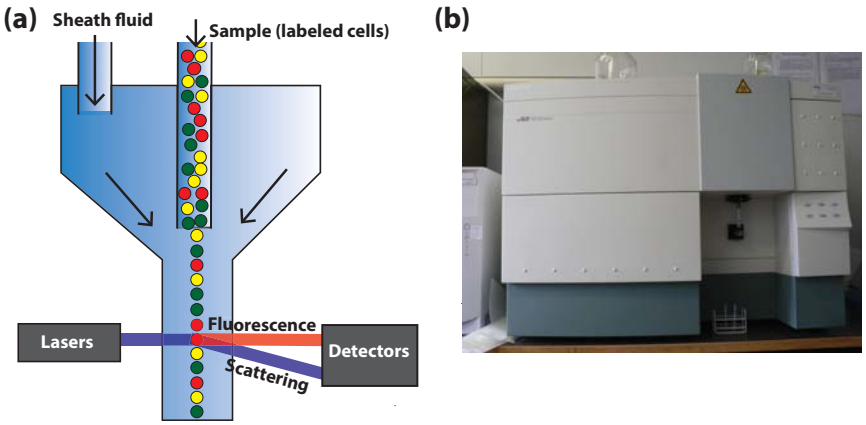

Figure 2.5: (a) Schematic of the working principle of a conventional flow cytometer. (b) Picture of a commercial flow cytometer.

throughput of more than thousands of cells per second and allow for fluorescence measurements in several colors (up to 10 colors).

Apart from the conventional systems, flow cytometers that use different schemes for cell detection or focusing have been demonstrated. For instance,

Imaging flow cytometers employ a high-speed camera and sophisticated data-processing algorithms to analyze cells at high-throughput [82]. Impedance flow cytometers, also called Coulter counters, analyze cells by measuring changes in electrical resistance using electrodes embedded in the fluidic channel [83]. Flow cytometers that carry out cell focusing by acoustics instead of sheath flows have been recently commercialized, and are poised to provide a better performance and solve clogging problems that occur in sheath flow-based devices [84]. Moreover, the biomedical laboratory has incorporated cytometers with additional features. For example, FACS (fluorescence-activated cell sorting) are devices that, in addition to cell analysis, can perform cell sorting by encapsulating the cells into charged droplets and deflecting them with electrostatic forces triggered by fluorescence measurements [85].

The latest research in flow cytometry points towards high-throughput and label-free analysis that could provide new insights to characterize cells. For instance, Raman flow cytometry [86] and Deformability flow cytometry [87] represent a promising direction that could enable identifying diseases at earlier stages, as well as overcoming the limitations of cell labeling mechanisms.

2.3.2 Micro-flow cytometers

To date, flow cytometers are only available at advanced medical facilities, since, as mentioned in the introduction, they are expensive, bulky (Fig. 2.5(b)), and complex machines that required trained personnel to operate. This poses a disadvantage for patients at locations where this instrument is not available. In this case, samples are sent to a core medical laboratory to be analyzed, which delays obtaining the information needed for deciding the most suitable treatment and could lead to sample deterioration during the delivery time. A significant amount of effort is being made to miniaturize flow cytometers in order to obtain portable units that can be used in point-of-care applications. Systems based on lab-on-a-chip and optofluidics (i. e. micro-flow cytometers) [88, 89] have been demonstrated by using embedded optical fibers [90, 91] or slab waveguides [92] to integrate optics into microfluidic chips. However, despite recent advances, current microsystems are still slower and less versatile than traditional instruments.

The all-silica fiber microflow cytometer reported in **Paper III** could represent the basis for a point-of-care flow cytometer with performance comparable to commercial systems. It integrates circular capillaries for cells and particles transport and a double-clad optical fiber for detection. Elasto-inertial microfluidics, discussed in the next section, is used to focus particles or cells into a single-stream at the center of a capillary in order to optimize detection.

2.4 Microfluidics

In **Paper III**, we employed Elasto-Inertial microfluidics to control the transveral position of particles flowing in a capillary. In this section, we present a theoretical background of microfluidics, Inertial microfluidics, and Elasto-inertial microfluidics.

2.4.1 Navier-stokes equation

The motion of a fluid is governed by the continuity equation and the Navier-Stokes (NS) equation, which describe conservation of mass and momentum, respectively [18, 19]. For an incompressible Newtonian fluid, the continuity equation is

$$\vec{\nabla} \cdot \vec{u} = 0, \tag{2.9}$$

and the NS equation is

$$\rho \left(\frac{\partial \vec{u}}{\partial t} + \vec{u} \cdot \nabla \vec{u} \right) = -\nabla p + \vec{\nabla} \cdot \left[\mu \left(\nabla \vec{u} + (\nabla \vec{u})^T \right) - \frac{2}{3} \mu \left(\vec{\nabla} \cdot \vec{u} \right) \vec{I} \right] \tag{2.10}$$

The parameter ρ is the fluid density, $\vec{u}$ is the flow velocity, p is the pressure, μ is the dynamic viscosity of fluid, and $\vec{I}$ is the identity matrix. The term on the left-hand side in the NS equation represents the inertial forces, whereas the first and the second term on the right-hand side correspond to the pressure and viscous forces, respectively. For a given geometry, the NS equation and the continuity equations can be solved by numerical methods such as computational fluidic dynamics (CDF) [93]. However, for some simple cases, these equations admit analytical solutions. For instance, the velocity profile for a two-dimensional steady-state and highly viscous flow between two parallel plates is [18]

$$u(y) = \frac{1}{2\rho\mu}(y^2 - d^2)\frac{dp}{dx}, \tag{2.11}$$

where $2d$ is the width of the channel. In this case, the velocity profile is parabolic, as shown in Fig. 2.6. The velocity is maximum at the channel center and minimum at the walls. The same parabolic profile is obtained for three-dimensional channels with rectangular and circular cross section. In general, this type of flow is known as laminar and is characterized by the fluid traveling in regular paths, without lateral mixing of streamlines. In contrast, a flow that shows abrupt and irregular changes in velocity and trajectory is known as turbulent flow [18].

The Reynold number Re is an important parameter to discriminate whether a flow is laminar or turbulent. This non-dimensional number represents the ratio

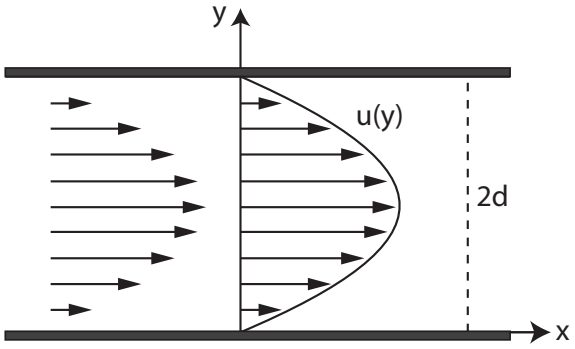

Figure 2.6: Parabolic flow profile between two parallel plates (Laminar flow).

between inertial forces and viscous forces, and is calculated by

$$Re = \frac{\rho U D_h}{\mu}, \tag{2.12}$$

where U is the average fluid velocity and D_h is hydraulic diameter of the channel. For $Re < 2300$, the flow tends to be laminar, whereas for $Re > 2300$ is expected to see a turbulent behavior [18]. Eq. 2.12 indicate that the flow would be laminar for low velocities, high viscocity, or channels with small dimension (microfluidics). It is important to note that for $Re << 1$, the effect of the inertial term of the Navier-Stokes equation can be neglected since it is much smaller than the effect of the viscous term.

2.4.2 Inertial microfluidics

Inertial microfluidics is a field that deals with particles flowing in microchannels in conditions where inertial forces affect the lateral position of the particles [94–97]. In flows at Reynold numbers between 1 and 100, the inertial term of the Navier-Stokes equation becomes relevant and gives rise to lateral migration of particles. The phenomenon was first observed for $1\ \mathrm{mm}$ spherical particles flowing in a cylindrical pipe of $1\ \mathrm{cm}$ diameter [98]. Particles moved laterally converging to an annulus with a radius 0.6 times the pipe radius [98], as shown in Fig. 2.7(a). Inertial migration of particles has been explained by the combined effect of two forces; a shear-gradient lift force that pushes the particle towards the channel walls, and a wall-induced lift force that pushes the particle to the channel center. The shear-gradient lift force F_{SG} arises from the difference in flow velocity on either side of the particle due to the parabolic flow profile, and is calculated by [96, 97]

$$F_{SG} = \frac{C_{SG}\rho U_m^2 a^3}{D_h} \tag{2.13}$$

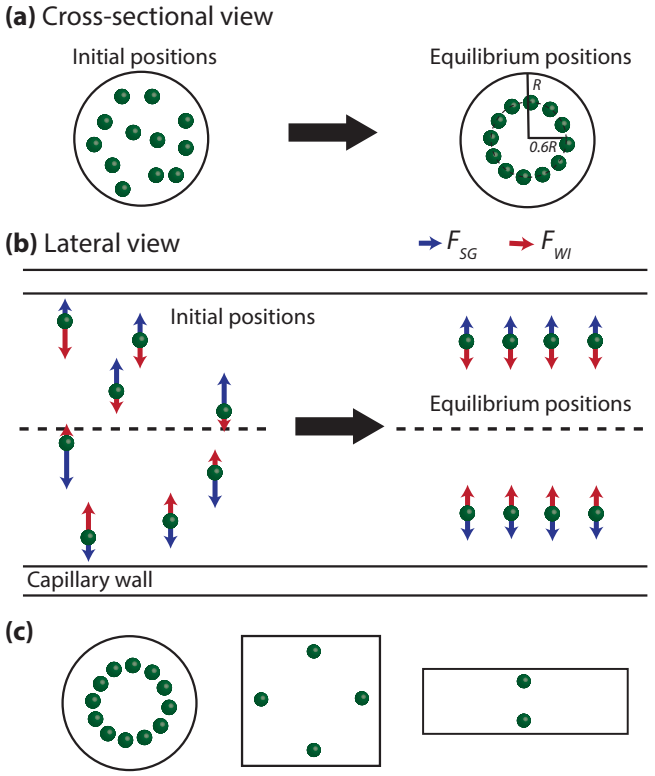

Figure 2.7: Inertial focusing in a capillary pipe. (a) Cross-sectional view. (b) Lateral view. (c) Equilibrium position for channels of different cross-section.

C_{SG} is a non-dimensional coefficient that depends on the Reynolds number and the transversal position of the particle, ρ is the fluid density, U_m is the maximum flow velocity, a is the particle diameter, and D_h is the hydraulic diameter of the channel. As the particle approaches the wall due to the shear-gradient lift force, the pressure becomes higher on one side of the particle giving rise to a second force that repels the particle away from the walls. This wall-interaction lift force F_{WI} is given by

$$F_{WI} = \frac{C_{WI}\rho U_m^2 a^6}{D_h^4}, \tag{2.14}$$

where C_{WI}, similarly to C_{SG}, is a non-dimensional coefficient with dependence on the Reynold number and particle lateral position [97]. The balance between the shear-gradient life force and the wall-induced lift force leads the particles to focus at equilibrium positions in the microchannel. This is shown schematically in Fig. 2.7(b). The focusing positions depend on the geometry of the channel. As mention above, particles concentrate at an annulus for a cylindrical pipe. In the case of square and high-aspect-ratio rectangular straight channels, focusing occurs at four positions at the center of each wall and two positions at the center of the wider walls, respectively (Fig. 2.7(c)) [95].

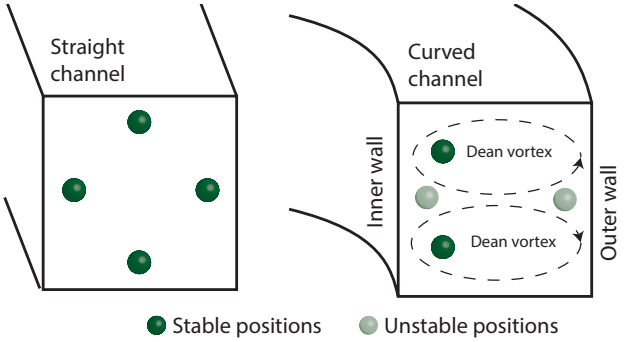

Figure 2.8: Inertial focusing in (a) square straight channels (b) curved straight channel.

Microchannels with curved geometries have been employed to control the focusing distribution of particles. The curvature of a microchannel induces a secondary flow (i. e. Dean flow) that modifies the equilibrium positions found in straight channels [96, 97]. The Dean flow is a consequence of the fluid inertia and the alteration of parabolic flow profile by the channel curvature. When the fluid enters a curved microchannel, the central streamline, which moves faster and possesses a higher momentum, shifts towards the concave outer wall. This causes recirculation of fluid due to conservation laws which results in two counter-rotating vortices (Dean vortices), as depicted in Fig. 2.8. These vortices are responsible for disturbances in the focusing positions of particles. For instance, in a curved channel with a square cross-section, the Dean flow would make particles to focus at two stable equilibrium position closer to the inner wall, as shown in Fig. 2.8. The Dean flow is characterized by the Dean number De and a Dean drag force F_D. The Dean number is a non-dimensional number that depends on Re, D_h, and the curvature of the channel R [97],

$$De = Re\sqrt{\frac{D_h}{2R}} \tag{2.15}$$

The Dean drag force depends on the average velocity of the Dean flow U_D, the particle size, and the dynamic viscosity of the fluid,

$$F_D = 6\pi\mu a U_D \tag{2.16}$$

The magnitude of U_D can be approximated by $U_D = 1.8 \times 10^{-4} De^{1.63}$ [99]. Microchannel with various curved geometries such as spiral and serpentine-shaped have been used for engineering the equilibrium positions. Inertial microfluidics has led to several life-science applications, for instance, bacteria and cell separation [100, 101], and sheath-less focusing of cells for flow cytometry [102, 103].

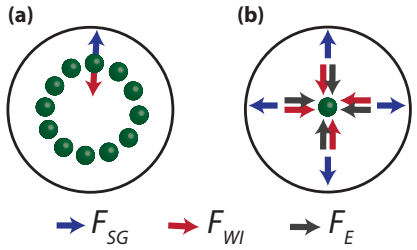

Figure 2.9: Particle focusing in a cylindrical channel. (a) Inertial microfluidics. (b) Elasto-inertial microfluidics.

2.4.3 Elasto-Inertial microfluidics

In addition to curved geometries, the focusing positions of particles can be controlled by using Elasto-inertial microfluidics [104–111]. This is a method that exploits fluid inertia and elastic forces that appear when particles flow in a non-Newtonian viscoelastic fluid. This fluid is usually made by adding a polymer (elasticity enhancer) to the solution. The elasticity of a non-Newtonian fluid is characterized by a non-dimensional numbed called Weissenberg number Wi [110, 111],

$$Wi = \lambda_r \frac{2U}{w} \tag{2.17}$$

The parameter λ_r is the relaxation time of the viscoelastic fluid, U, as mentioned before, is the average velocity of the fluid, and w is the channel width. The quantity $2U/w$ corresponds to the characteristic shear rate of the fluid. The elastic force F_E that a particle experiences in a non-Newtonian fluid depends on the particle diameter and the first normal stress difference $N1$ [110, 111],

$$F_E \sim a^3 \nabla N_1 \tag{2.18}$$

This elastic force, added to the inertial forces (shear gradient lift and wall-induced lift), results in a modification of the focusing positions of the particles. For instance, it has been shown that, with the aid of the elastic force, particle focusing can be achieved in a single-stream at the center of the cylindrical channel, instead of the annular distribution found in Inertial microfluidics [106]. This behavior, illustrated in Fig. 2.9, is explained by the fact that elastic force points towards the center of the channel where N_1 is minimum.

Paper III presents an experimental characterization of particle focusing in cylindrical capillaries by Elasto-inertial microfluidics for various Reynolds number, particle size, and capillary diameter. This study is done by taking long-exposure fluorescence images of flowing particles.

2.5 Liquid crystals devices

In **Paper IV** and **V**, we propose that the electrically induced alignment of gold nanorods in suspension can provide faster response times than liquid crystals devices for light intensity modulation. In this section, we present a brief description of the working principle of liquid crystal devices and a theoretical background of their dynamic properties. This theory is not discussed in the **Papers IV-V**. However, we find useful to include it here in order to understand the limitations of liquid crystals devices for fast electro-optical modulation and motivate research on plasmonic nanorods suspensions as a feasible alternative.

2.5.1 Liquid crystals devices: Basics

Liquid crystals (LCs) is a phase of matter where anisotropic molecules have fluidic properties like liquids, however, they possess an intrinsic order similar to crystals [112]. LCs molecules can be aligned with an external electric field, allowing for the control of the light transmitted through them [113–115]. This capability has led to groundbreaking technology such as flat displays for computers and smartphones. The commercial use of LCs for electro-optical modulation started off with the development of the twisted-nematic liquid crystal (TN-LC) devices [113]. These devices exploit the nematic phase of LCs where molecules tend to self-align with their long axes in the same direction. Fig. 2.10 illustrates the working principle of a TN-LC cell. Nematic liquid crystal is placed inside a cell composed of two parallel glass plates. The glass plates are bonded to alignment layers that are used to induce planar alignment to the LC molecules near the surface (surface anchoring). The alignment layers can be obtained, for instance, by using a surface with parallel micro-grooves [116]. In Fig. 2.10, the alignment layers cause the LC molecules that are near the first and second glass plate to align in the z- and x-direction, respectively. The orientation of the molecules in the cell follows a smooth transition, organizing themselves into a helix, as seen in Fig. 2.10(a). Polarizers $P1$ and $P2$ are placed on either side of the cell at orientations z and x respectively (crossed polarizers). After $P1$, light enters the cell with its polarization in the z-direction, parallel to the orientation the molecules anchored to the first glass plate. As the light propagates through the cell, its polarization gradually rotates to the x-direction due to the birefringence of the LC molecules and their helicoidal distribution. Hence, light exiting the cell will be polarized at the same orientation of $P2$ and it will be transmitted, Fig. 2.10(a). The glass plates are coated with a transparent conductive material. If a voltage is applied between the two plates, the long axis of LC molecules will align to the electric field along y-direction, as seen in Fig. 2.10(b). In this case, the polarization is not rotated, and light will be absorbed by $P2$. After switching off the voltage, the LC molecules will return to their helicoidal distribution and light will be once again transmitted. This alignment of LC molecules under an electric field is known as Freedericksz-transition.

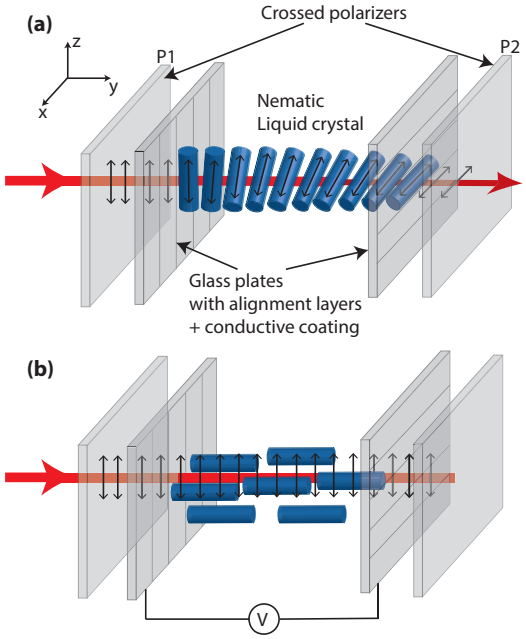

Figure 2.10: Working principle of a TN-LC cell. (a) No voltage applied. (b) Voltage V applied. $P1$ and $P2$ are polarizers oriented at the z- and x-direction, respectively.

2.5.2 Liquid crystals devices: Response time

The mathematical treatment presented in this section is based on the reference [115] *"Liquid crystal displays: fundamental physics and technology"*.

The major limitation of LC crystal devices is the slow response time, which has constrained potential electro-optic applications. The Ericksen-Leslie dynamic continuum theory [115, 117] can be used to study the characteristic response times of LC devices and their limitations. For simplicity, consider the case when the molecules are aligned along the x-direction on both surfaces and an electric field of magnitude E is applied in the y-direction, $\vec{E} = E\hat{y}$. Thus, the electric field only causes the molecules to twist on the xy-plane (in-plane switching), as seen in Fig. 2.11. Consider also that the alignment of molecules located at surfaces does not change when the electric field is applied (i. e. strong anchoring condition).

The time evolution of the twist angle ϕ, Fig. 2.11, is governed by the Ericksen-Leslie equation [115],

$$\gamma_1 \frac{\partial \phi}{\partial t} = K_{22} \frac{\partial^2 \phi}{\partial z^2} + \epsilon_0 \Delta\epsilon E^2 \cos\phi \sin\phi \tag{2.19}$$

γ_1 and K_{22} are the viscosity and the twist elastic constant of the liquid crystal, respectively. ϵ_0 is the vacuum permittivity and $\Delta\epsilon$ is the dielectric anisotropy. Eq. 2.19 represents an over-damped system where the first term of the right-hand side comes from the elastic energy and the second term from the torque produced

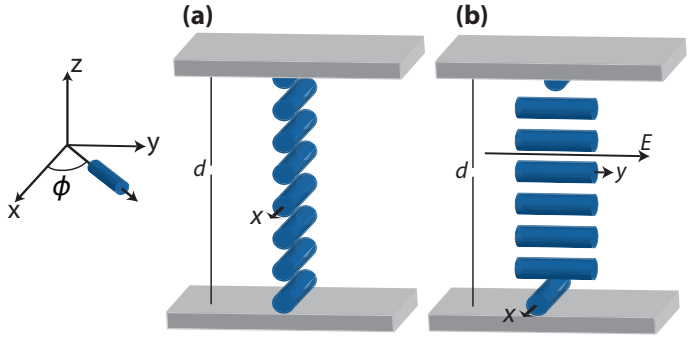

Figure 2.11: In-plane twist geometry. (a) No electric field; LC molecules aligned in the x-direction (b) Molecues aligned by an electric field along the y-direction.

by the electric field due to the dipole moment of the LC molecules. Using a small angle approximation, $\phi << 1$, Eq. 2.19 can be linearized by substituting $\sin\phi \approx \phi$ and $\cos\phi \approx 1$,

$$\gamma_1 \frac{\partial\phi(z,t)}{\partial t} = K_{22}\frac{\partial^2\phi(z,t)}{\partial z^2} + \epsilon_0\Delta\epsilon E^2\phi(z,t) \tag{2.20}$$

Considering the initial conditions $\phi(z,0) = \phi_0$ and $\phi_0(0) = \phi_0(d) = 0$, where d is thickness of the cell. The solution of Eq. 2.20 can be obtained in term of Fourier series as

$$\phi(z,\tau) = \sum_{n=1}^{\infty} A_n \sin\left(\frac{\pi n z}{d}\right) e^{-t/\tau_n}, \tag{2.21}$$

where the Fourier coefficients A_n are

$$A_n = \frac{2}{d}\int_0^d \phi_0(z)\sin\left(\frac{\pi n z}{d}\right) dz \tag{2.22}$$

Replacing Eq. 2.21 in Eq. 2.20, it is found that the relaxation time of the n-th Fourier mode is

$$\tau_n = \frac{\gamma_1}{\epsilon_0\Delta\epsilon\,(n^2E_{th}^2 - E^2)} \tag{2.23}$$

The parameter E_{th} is the threshold electric field,

$$E_{th} = \frac{\pi}{d}\sqrt{\frac{K_{22}}{\epsilon_0\Delta\epsilon}} \tag{2.24}$$

E_{th} is a common parameter in Freedericksz transition-based devices [115] and measures the relative importance of the two terms on the right-hand side of Eq. 2.20. If $E < E_{th}$, then $\tau_n > 0$ and ϕ decays exponentially to zero, therefore

alignment of molecules does not take place, as seen in Eq. 2.21. Contrarily, if $E > E_{th}$, then $\tau_n < 0$, and ϕ rapidly increases, causing LC molecules to align towards the direction of the electric field. For $E > E_{th}$ the on-time τ_{on} of the LC molecules is defined as

$$\tau_{on} = -\tau_1 = -\frac{\gamma_1}{\epsilon_0 \Delta\epsilon \left(E_{th}^2 - E^2\right)}. \tag{2.25}$$

This expression can be written in terms of the voltage applied, $V = Ed$,

$$\tau_{on} = \frac{\gamma_1 d^2}{\pi^2 K_{22} \left(V^2/V_{th}^2 - 1\right)}, \tag{2.26}$$

where the substitution $\epsilon_0 \Delta\epsilon V_{th}^2 = \pi^2 K_{22}$ was used (Eq. 2.24). Switching off the electric field causes the molecules to decay to their undisturbed initial state in a time τ_{off} (off-time) given by

$$\tau_{off} = \frac{\gamma_1 d^2}{\pi^2 K_{22}} \tag{2.27}$$

The response time of the LC device can be analyzed with Eq. 2.26 and Eq. 2.27. While the on-time can be arbitrarily reduced by increasing the voltage applied, the off-time, since it only depends on the physical properties of the LC and cell thickness, cannot be easily improved. For instance, if $\gamma_1 = 0.1\ \mathrm{N\,s\,m^{-2}}$, $K_{22} = 10^{-11}\ \mathrm{N}$ and $d = 5\ \mu\mathrm{m}$, the off-time is $\tau_{off} = 25\ \mathrm{ms}$. The slow off-time limits the overall response time of a Freedericksz transition-based LC devices to the order of milliseconds. For the parameters mentioned above and $\Delta\epsilon = 12.7$, the threshold electric field, obtained form Eq. 2.24, is $E_{th} = 0.19\ \mathrm{V\,\mu m^{-1}}$. In the next section, the theoretical background for the alignment of nanorods under an electric field is presented. As it will be shown, this nanorods-based system presents a much faster response time than liquid crystals for electrical modulation of light intensity.

2.6 Plasmonic properties of nanorods and electrically induced alignment

In **Papers IV** and **V**, we present all-fiber optofluidic devices that allow orienting gold nanorods in suspension with an electric field and studying their optical properties. As mentioned before, this work is motivated by the fact that a scheme based on nanorod suspensions could enable electro-optical modulation with much faster response times than liquid-crystal devices. In addition, this scheme could exploit the plasmonic properties of gold nanorods such as tunable optical absorption.

This section introduces surface plasmon resonances of nanorods and describes a theoretical model with corresponding numerical simulations for the electrically-induced alignment of nanorods in suspension. This model is used to analyze and

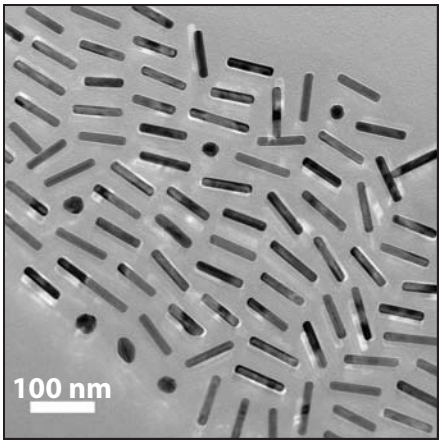

Figure 2.12: TEM image of gold nanorods of length $100\ \mathrm{nm}$ and width $25\ \mathrm{nm}$. Picture provided by Jake Fontana, NRL

fit the experimental data in **Paper IV**, obtaining optical and dynamics parameters. **Papers IV** and **V** are summarized in Sec. 3 and reprinted in the end of this thesis.

2.6.1 Surface plasmon resonances of nanorods

Metallic nanorods (NRs) have been exploited in a variety of fields like spectroscopy [118], biosensing [119], and optical tracking [120]. Fig. 2.12 shows a TEM image of gold nanorods of length $100\ \mathrm{nm}$ and width $25\ \mathrm{nm}$. As mentioned in Sec. 1.3, metallic nanoparticles exhibit surface plasmon resonances when they interact with visible light [41, 42]. Metallic nanorods present a longitudinal surface plasmon resonance (LSPR) and a transversal surface plasmon resonance (TSPR) associated to oscillations in the parallel and perpendicular direction [121], as illustrated in Fig. 2.13. The Maxwell-Garnett (MG) model can be used to calculate the intrinsic absorption coefficients of metal nanorods [122, 123],

$$\mu_{\parallel(\perp)} = \frac{2\pi \mathrm{Im}(\epsilon)}{\lambda n_h} \left| \frac{\epsilon_h}{\epsilon_h + L_{\parallel(\perp)} (\epsilon - \epsilon_h)} \right|^2 \tag{2.28}$$

The MG model is valid for particles smaller that the optical wavelength λ, where absorbance is dominant over scattering. The subscript $\parallel$ $(\perp)$ indicates the direction parallel (perpendicular) to the long axis of the nanorod. The parameter ϵ is the complex dielectric function of gold, ϵ_h and n_h are the dielectric constants and refractive index of the host medium respectively, and $L_{\parallel(\perp)}$ are the depolarization factor. An approximation of the complex dielectric function ϵ can be obtained from the Drude model [42],

$$\epsilon = 1 + \epsilon_{inter} + \frac{\omega_p^2}{\omega^2 + i\beta\omega}, \tag{2.29}$$

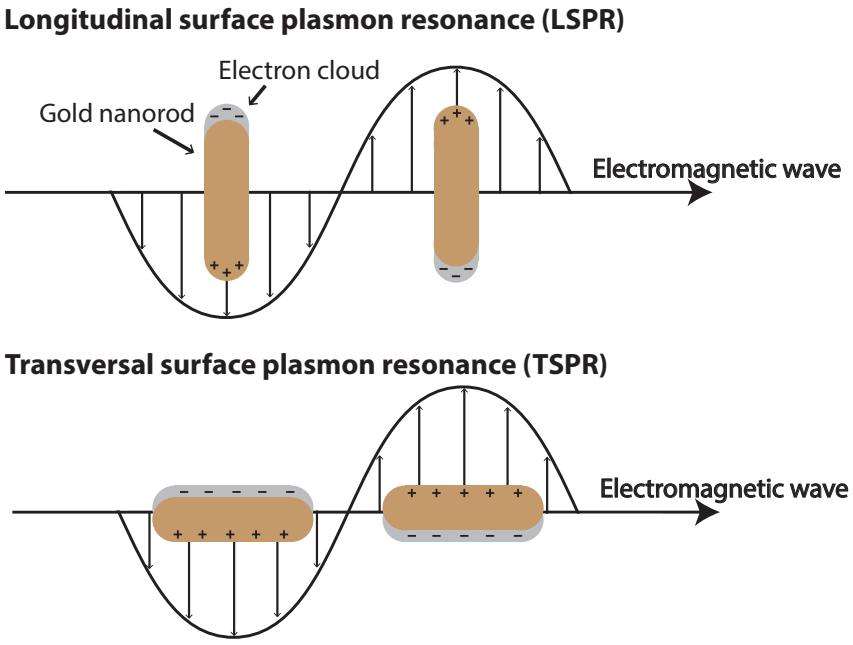

Figure 2.13: Schematic of the longitudinal and transversal surface plasmon resonances of nanorods

where the term, ϵ_{inter}, is a constant that represents the contribution from interband electron transitions. The frequency-dependent term is the contribution from intraband electron transitions, ω is optical frequency, ω_p is the plasma frequency of gold, and β is the damping constant [121]. In gold, Eq. 2.29 is valid for visible frequencies, where ϵ_{inter} can be considered a constant. Due to the finite size of the nanoparticles, β differs from its bulk value and depends on the particle size [42]. Approximating the nanorod to a prolate ellipsoid, the depolarization factors $L_{\parallel(\perp)}$ are given by [123, 124]

$$\begin{aligned} L_{\parallel} &= \frac{b^2}{a^2-b^2}\left[\frac{a}{2\sqrt{a^2-b^2}}\ln\left(\frac{a+\sqrt{a^2-b^2}}{a-\sqrt{a^2-b^2}}\right)-1\right], \\ L_{\perp} &= \frac{1-L_{\parallel}}{2}, \end{aligned} \tag{2.30}$$

where a and b are the long and short semi-axis of the ellipsoid which correspond to half the nanorods length L and width W, respectively. Fig. 2.14(a) shows the total absorption coefficient of a nanorod $\mu_T = (\mu_{\parallel} + \mu_{\perp})/2$ as a function of the wavelength. The parameters used in the simulation are listed in Table 1 and correspond to the experimental conditions described in **Paper IV**, where gold nanorods are suspended in toluene. These parameters result in an optical response with a larger LSPR peak center at 742 nm and a smaller TSPR peak centered at 532 nm. One of the properties that makes metallic nanorods interesting is that their optical response can be tuned by adjusting the size, shape, medium and material. For in-

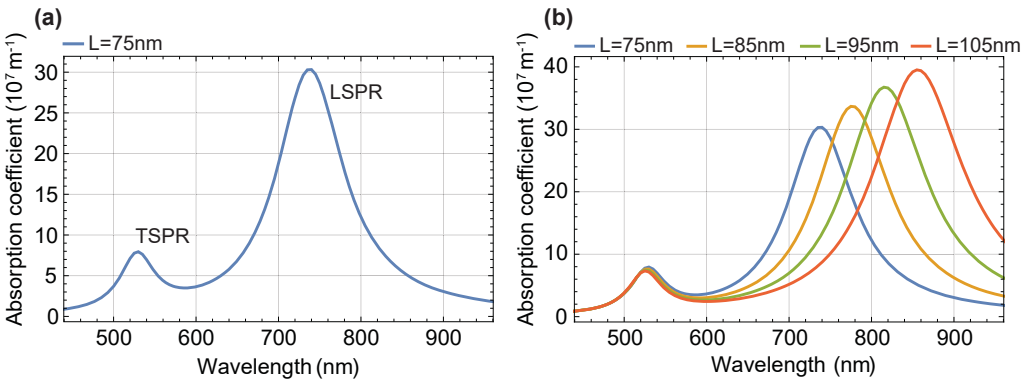

(h)

Figure 2.14: (a) Simulation of the total absorption coefficient as a function of the wavelength. (b) Shift of the LSPR for nanorods of different length L. Parameter used are listed in Table 2.1.

stance, increasing the nanorod length modifies the depolarization factors causing a shift of the LSPR towards the infrared, as illustrated in Fig. 2.14(b).

Parameter	Value
L	75, 85, 95, 105 nm
W	25 nm
n_h	1.49 (toluene)
ϵ_h	2.38 (toluene)
ϵ_{inter}	13.5
ω_p	14.9×10^{15} rad s^{-1}
β	3.4×10^{14} rad s^{-1}

Table 2.1: Parameter used for simulation of Fig. 2.14. Values correspond to the experimental conditions presented in **Paper IV**.

2.6.2 Motion equations for a Brownian particle

To develop a theory for the electrically-induced alignment of nanorods suspended in a liquid medium, the first step is to consider the Brownian motion of a particle immersed in a fluid. The one-dimensional Newton's motion equation for the velocity of Brownian particle $v(t)$ is

$$m\frac{d\vec{v}}{dt} = \vec{F}(t), \tag{2.31}$$

$\vec{F}(t)$ is the time-dependent total force determined by a friction force proportional

to the velocity of the particle $-\gamma\vec{v}(t)$ and a random force $\vec{\xi}(t)$ due to the collisions of the particle with the molecules in the fluid (i.e. background or white noise) [125, 126]. The coefficient γ is the dynamic viscosity and is given by the Stoke law (for a spherical particle, $\gamma = 6\pi\eta r$, where η is the medium viscosity and r is the particle radius). The random force $\vec{\xi}(t)$ is a stochastic function with known statistical properties [126]. Generally, the equations of motion of the Brownian particle can be expressed as

$$\begin{aligned} \frac{d\vec{x}(t)}{dt} &= \vec{v}(t) \\ \frac{d\vec{v}(t)}{dt} &= -\gamma\vec{v}(t) + \vec{\xi}(t) + \vec{F}_{EX}(\vec{x},t), \end{aligned} \tag{2.32}$$

where $x(t)$ is the particle position and $\vec{F}_{EX}(\vec{x},t)$ is any external force acting on the particle. In the case of the electrical-induced alignment of nanorods, as discused below, this force is calculated from the torque produced by the electric field. In the limit of strong friction (high viscosity) the inertial force $d\vec{v}(t)/dt$ can be neglected, obtaining

$$\gamma\frac{d\vec{x}(t)}{dt} = \vec{\xi}(t) + \vec{F}_{EX}(\vec{x},t) \tag{2.33}$$

This equation is known Langevin equation [125], and corresponds to an stochastic equation that depends on the random function $\vec{\xi}$ and the deterministic external force $\vec{F}_{EX}$. An approach to solve Eq. 2.33 relies on using the Fokker-Plank equation [125], which describes the time variation of the probability distribution $P(x,t)$ of a degree of freedom x of a particle under the influence of friction forces, external forces, and random forces,

$$\frac{\partial P(x,t)}{\partial t} = D\left[\frac{\partial^2 P(x,t)}{\partial x^2} + \frac{1}{kT}\frac{\partial}{\partial x}\left(F_{EX}(x,t)P(x,t)\right)\right] \tag{2.34}$$

$D = \gamma/kT$ is the diffusion coefficient and defines the characteristic relaxation time of the system, k is the Boltzmann constant, and T is the temperature. $P(x,t)$ is normalized as

$$\int P(x,t)dx = 1 \tag{2.35}$$

The Fokker-Plank equation can be derived directly from the Langevin equation by considering that the background noise has a Gaussian probability distribution,

$$P_{noise}(x,t) = \frac{1}{\sqrt{4\pi Dt}}\exp\left(-\frac{x^2}{4Dt}\right), \tag{2.36}$$

which satisfies the diffusion equation

$$\frac{\partial P_{noise}(x,t)}{\partial t} = D\frac{\partial^2 P_{noise}(x,t)}{\partial x^2} \tag{2.37}$$

2.6.3 Einstein-Smoluchowski (ES) equation

Consider the case of a nanorod being aligned by an electric field $\vec{E}(t)$ applied in z direction. The torque exerted on the nanorods by the electric field is given by [123, 124, 127],

$$\vec{T} = \epsilon_0 \left(\vec{\alpha}\vec{E}\right) \times \vec{E}. \tag{2.38}$$

ϵ_0 is the vacuum permittivity and $\vec{\alpha}$ is the polarizability tensor of the nanorod. The quantity $\vec{\alpha}\vec{E}$ corresponds to the dipolar moment. To study the rotation of the nanorod, it is convenient to transform the system to spherical coordinates. The polarizability tensor can be written as

$$\vec{\alpha} = \alpha_{\parallel}\hat{1}\hat{1}^T + \alpha_{\perp}(\hat{2}\hat{2}^T + \hat{3}\hat{3}^T), \tag{2.39}$$

where,

$$\begin{aligned}
\hat{1} &= \sin\theta\cos\phi\hat{x} + \sin\theta\sin\phi\hat{y} + \cos\theta\hat{z}, \\
\hat{2} &= \cos\theta\cos\phi\hat{x} + \cos\theta\sin\phi\hat{y} - \sin\phi\hat{z}, \\
\hat{3} &= -\sin\phi\hat{x} + \cos\phi\hat{y},
\end{aligned} \tag{2.40}$$

are the unit vector in spherical coordinates restricted to the surface of a unit sphere (radial coordinate, $r = 1$). As illustrated in Fig. 2.15(a), θ is the polar angle between the nanorod long axis of the nanorod and the z-axis, ϕ is the azimuthal angle between the x-axis and the projection of the nanorod long axis onto the xy-plane. The values for the polarizabilities $\alpha_{\parallel}$ and $\alpha_{\perp}$ are given by [123],

$$\alpha_{\parallel(\perp)} = \frac{\varepsilon_{\parallel(\perp)} - \varepsilon_h}{\varepsilon_h + L_{\parallel(\perp)}\left(\varepsilon_{\parallel(\perp)} - \varepsilon_h\right)}V, \tag{2.41}$$

where, as mentioned above, the subscript $\parallel$ $(\perp)$ represents the direction parallel (perpendicular) to the long axis of the nanorod. V is the volume of a nanorod, $\varepsilon_{\parallel(\perp)}$ are the real dielectric constants of the nanorods, and ε_h is the dielectric constant of the host medium. Using Eq. 2.39 and Eq. 2.40, the torque, Eq. 2.38, can be expressed as

$$\vec{T} = \Delta\alpha\cos\theta\sin\theta\epsilon_0 E^2(t)\hat{3} \tag{2.42}$$

The parameter $\Delta\alpha$ is the anisotropy in polarizability defined as $\Delta\alpha = \alpha_{\parallel} - \alpha_{\perp}$. In

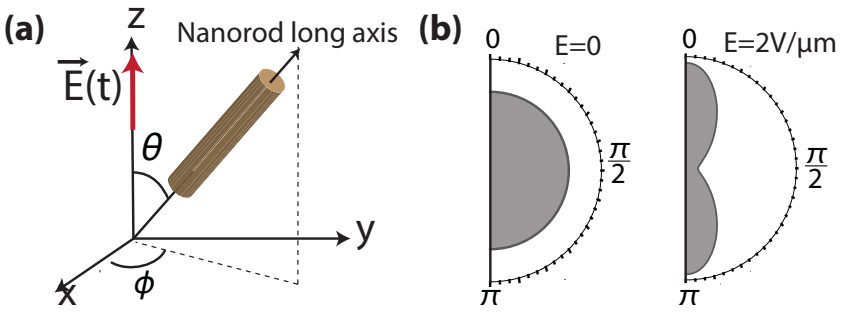

Figure 2.15: (a) Schematic of a nanorod under an electric field along the z-direction. (b) Simulation of the probability distribution $P(\theta, t)$ for $E = 0$ and $E = 2\ \mathrm{V\,\mu m^{-1}}$. The parameter used for the simulation (b) are $D = 5000\ \mathrm{s^{-1}}$ and $\Delta\alpha = 1.2 \times 10^{-22}\ \mathrm{m^3}$

order to study the effect of the torque on the orientation of nanorods in suspension (Brownian particles), we use the Fokker-Plank equation (Eq. 2.34) expressed in spherical coordinates,

$$\frac{\partial P(\theta,t)}{\partial t} = D\left[\frac{1}{\sin\theta}\frac{\partial}{\partial\theta}\left(\sin\theta\frac{\partial P(\theta,t)}{\partial\theta}\right) + \frac{1}{kT}\frac{1}{\sin\theta}\frac{\partial}{\partial\theta}\left(\sin\theta F_{EX}(\theta,t)P(\theta,t)\right)\right], \tag{2.43}$$

where the probability distribution is invariable respect to the azimuthal angle ϕ. Applying $F_{EX} = |\hat{1} \times \vec{T}|$ (Eq. 2.42) and simplifying

$$\frac{\partial P(\theta,t)}{\partial t} = D\left[\frac{1}{\sin\theta}\frac{\partial}{\partial\theta}\left(\sin\theta\frac{\partial P(\theta,t)}{\partial\theta} + \frac{\Delta\alpha\epsilon_0 E^2(t)}{kT}P(\theta,t)\sin^2\theta\cos\theta\right)\right] \tag{2.44}$$

This form of the Fokker-Plank equation is known as Einstein-Smoluchowski (ES) equation [124, 127–129]. In this case, D is the rotational diffusion constant. The probability distribution $P(\theta, t)$ can be obtained by numerically solving the ES equation. If $E = 0$, there is no nanorods alignment and $P(\theta, t)$ is uniform. If $E > 0$, nanorods alignment takes place and $P(\theta, t)$ becomes peaked around 0 and π, as seen in Fig. 2.15(b).

2.6.4 Nanorods interacting with polarized light and electric fields

In this section, we study the optical response of the system by considering an ensemble of nanorods in suspension interacting with polarized light and an external electric field, as depicted in Fig. 2.16

The total absorption coefficient $\mu(t)$ of the system can be calculated as [123].

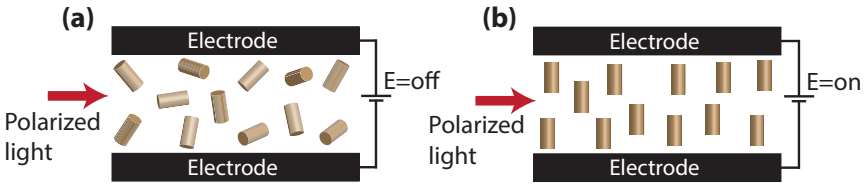

Figure 2.16: Schematic of a nanorod under an electric field. (a) Electric field off, nanorods are randomly oriented. (b) Electric field on, nanorods aligned

$$\mu(t) = \int_0^{2\pi} \int_0^{\pi} (A\mu_{\parallel} + B\mu_{\perp}) P(\theta, t) \sin\theta d\theta d\phi. \tag{2.45}$$

The parameter A corresponds to the square of the projection of the nanorod long axis in the direction parallel to the light polarization, and B corresponds to the sum of the squared projection of the nanorods on the two axes perpendicular to the light polarization. The projection is squared due to the inversion symmetry of nanorods. From Fig. 2.15, the Cartesian coordinates are

$$\begin{aligned} x &= \sin\theta\cos\phi \\ y &= \sin\theta\sin\phi \\ z &= \cos\theta \end{aligned} \tag{2.46}$$

If the polarization of the light is parallel to the direction of the electric field (z-axis), then $A = z^2$ and $B = x^2 + y^2$. Hence, the total absorption coefficient $\mu(t)$ is given by

$$\mu(t) = \int_0^{2\pi} \int_0^{\pi} \left(\mu_{\parallel}\cos^2\theta + \mu_{\perp}\sin^2\theta\right) P(\theta, t) \sin\theta d\theta d\phi \tag{2.47}$$

On the other hand, if the polarization of the light is perpendicular to the electric field, then $A = x^2$, $B = y^2 + z^2$, and therefore $\mu(t)$ is

$$\mu(t) = \int_0^{2\pi} \int_0^{\pi} \left[\mu_{\parallel}\sin^2\theta\cos^2\theta + \mu_{\perp}\left(1 - \sin^2\theta\cos^2\theta\right)\right] P(\theta, t) \sin\theta d\theta d\phi \tag{2.48}$$

Finally, the absorbance of the nanorods suspension $A(t)$ can be retrieved using the Lambert-Beer law [123]

$$A(t) = \mu(t) f l / \ln 10, \tag{2.49}$$

where l is the path length where the light interacts with the nanorods and f is the volume fraction of the nanorods in the suspension. To compute the absorption coefficient $\mu(t)$ and the absorbance $A(t)$, we calculate the probability distribution $P(\theta, t)$ from numerically solving the ES equation, and $\mu_{\parallel(\perp)}$ from the Eq. 2.28.

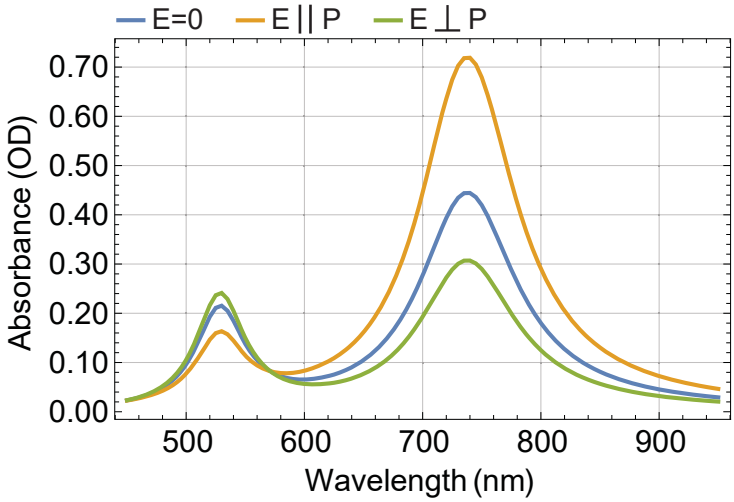

Figure 2.17: Simulation of the absorbance spectrum for a $2\ \mathrm{V\,\mu m^{-1}}$ electric field applied parallel or perpendicular to the polarization of the light. Parameters used in this simulators are listed in Table 2.1 with $L = 75\ \mathrm{nm}$, $D = 5000\ \mathrm{s^{-1}}$ and $\Delta\alpha = 5 \times 10^{-22}\ \mathrm{m^3}$

Fig. 2.17 shows the simulated absorbance spectra of nanorods aligned under an $2\ \mathrm{V\,\mu m^{-1}}$ electric field parallel and perpendicular to the polarization of the light. The parameters of this simulation are the same used for Fig. 2.14, Table 2.1 with $L = 75\ \mathrm{nm}$. In addition, the values for the rotational diffusion coefficient and anisotropy in polarizability are $D = 5000\ \mathrm{s^{-1}}$ and $\Delta\alpha = 5 \times 10^{-22}\ \mathrm{m^3}$. Without an electric field applied, the distribution of nanorods is random with the absorbance corresponding to the blue curve in Fig. 2.17. When the nanorods align with their long axis parallel to the electric field, orange curve in Fig. 2.17, the LSPR peak, centered at $742\ \mathrm{nm}$, increases, whereas the TSPR peak, centered at $532\ \mathrm{nm}$, decreases. Contrarily, when nanorods align perpendicular to the light polarization, green curve in Fig. 2.17, the LSPR decreases and the TSPR increases. Note that the change in absorbance for parallel alignment is twice the change in perpendicular alignment. This difference can be understood by approximating the random distribution as; (1) $1/3$ of the total number of nanorods oriented along the laser beam direction. (2) $1/3$ perpendicular to the laser polarization and perpendicular to the laser beam direction. (3) $1/3$ parallel to the laser polarization and perpendicular to the laser beam direction. Nanorods initially in (1) and (2) only contribute to a change in absorbance when the electric field aligns them parallel to the light polarization. In this case, the fraction of aligned nanorods goes from $1/3$ to 1, whereas for alignment in the direction perpendicular to the light polarization, the fraction goes from $2/3$ to 1.

In order to study the dynamic response of the system, we perform time-evolution simulations of nanorods aligned under a rectangular pulse electric field of $100\ \mu\mathrm{s}$. The light wavelength is fixed at $690\ \mathrm{nm}$, which is within the LSPR peak of the spectrum shown in Fig. 2.17. Fig. 2.18(a) and (b) show the case of polarization parallel and perpendicular to the electric field, respectively. The

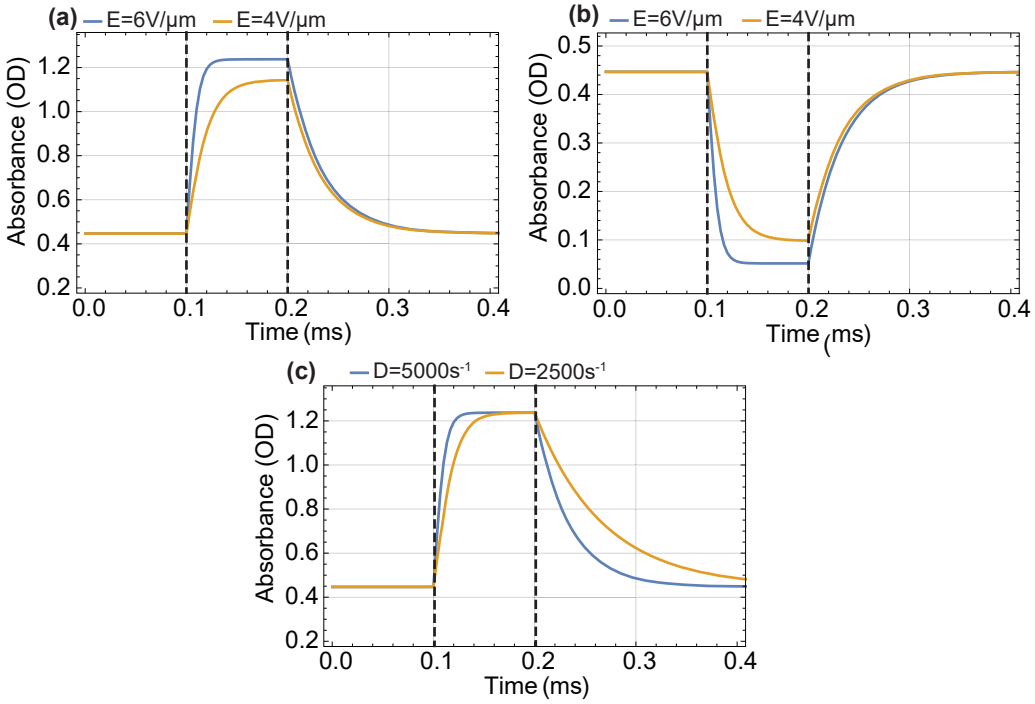

Figure 2.18: Simulation of the absorbance time-variation for a rectangular pulse electric field of 100 µs. Effect of the electric field magnitude for light polarized parallel (a) and perpendicular (b) to the electric field for $D = 5000\ \mathrm{s}^{-1}$. (c) Effect of the rotational diffusion D for light polarized parallel to the electric field, $E = 6\ \mathrm{V\,\mu m}^{-1}$. The parameter used in these simulations are listed in Table 2.1 with $L = 75$ nm and $\Delta\alpha = 5 \times 10^{-22}\ \mathrm{m}^3$. Dashed lines define the rectangular pulse.

on-time of the alignment depends on the magnitude of the electric field, the anisotropy in polarizability, and the rotational diffusion coefficient, according to the ES equation (Eq. 2.44). The on-time of the alignment decreases with increasing the magnitude of the electric field, as seen in Fig. 2.18(a,b) for $E = 4\ \mathrm{V\,\mu m}^{-1}$ and $E = 6\ \mathrm{V\,\mu m}^{-1}$. When the field is switched off, the orientation of the nanorods randomizes due to Brownian motion, thus the off-time only depends on rotational diffusion coefficient. This is seen in Fig. 2.18(c) for $D = 2500\ \mathrm{s}^{-1}$ and $D = 5000\ \mathrm{s}^{-1}$.

2.6.5 Nanorods alignment: characteristic times

As seen in Fig. 2.18, simulating the ES equation enables the analysis of the response time of the nanorods in suspension when aligned by an electric field. Additionaly, a direct expression for the on-time τ_{on} can be obtained from Langevin equation, Eq. 2.33, for the polar angle θ.

$$DkT\frac{d\theta(t)}{dt} = \Delta\alpha\cos\theta\sin\theta\epsilon_0 E^2 + \xi(t) \tag{2.50}$$

with $D = \gamma/kT$. For a sufficiently large electric field, the Brownian term $\xi(t)$ can be neglected and the on-time can be obtained by approximating the derivative to the ratio $\Delta\theta/\tau_{on}$, with $\Delta\theta = \pi/4$ [123].

$$\tau_{on} = \frac{\pi kT}{4D\Delta\alpha\epsilon_0 E^2} \tag{2.51}$$

The off-time τ_{off} of the system is related to the diffusion coefficient D by [130]

$$\tau_{off} = \frac{1}{6D} \tag{2.52}$$

The rotational diffusion coefficient D for a particle with aspect ratio (i.e length divided by width) AR can be calculated from hydrodynamic models [124, 131]

$$D = \frac{3kT}{\pi\eta L^3}\left(-\frac{0.05}{AR^2} + \frac{0.917}{AR} + \ln AR - 0.662\right) \tag{2.53}$$

For the nanorods used in **Paper III**, with $L = 75\,\mathrm{nm}$, $AR = 3$, $\eta = 0.55\,\mathrm{Pa\,s}$ (toluene), and $T = 293\,\mathrm{K}$), the theoretical rotational diffusion coefficient is $D = 11200\,\mathrm{s}^{-1}$ and, thus, the off-time is $\tau_{off} = 16\ \mu\mathrm{s}$. Such a response time is three orders of magnitude faster than traditional LC devices. The main reason for this improvement in response time is that the off-time of a diluted suspension of nanorods, contrarily to LC, does not depends of the length of the interaction cell (referred to as cell thickness in Sec. 2.5) .

Chapter 3

Summary of Papers I-V

This section presents a brief description of the all-fiber optofluidic devices reported in **Paper I-V** and summarizes the main results of each work. See publication reprints found in the end of this thesis for more detailed descriptions and additional results.

3.1 Paper I: A fiber optic system for detection and collection of micrometer-size particles

As mentioned in the introduction, the field of Lab-on-a-fiber is being developed to increase the functionality of optical fibers for ultimately performing advanced tasks in life-sciences. This technology could allow, by inserting a fiber into the human body, the in-vivo realization of studies that have been limited to in-vitro conditions, providing faster and more accurate diagnosis.

In **Paper I**, an optical fiber probe is presented capable of carrying out real-time monitoring and selective collection of individual microparticles from a liquid solution based on their fluorescence signal. This probe consists of a microstructured optical fiber which has either one or two holes along its cladding for particle aspiration, Fig. 3.1.

A schematic of the experimental setup is shown in Fig. 3.2(a). A laser emitting at $491\ \mathrm{nm}$ wavelength is used for particle excitation. A telecom fiber, provided with a $\approx 20\ \mathrm{nm}$ thick carbon-coating on the cladding surface, is fused to a piece of the microstructured fiber (Fig. 3.1). The carbon-coating fiber decreases background noise and, thus, increases the signal-to-noise ratio [132]. The excitation beam is launched into the fiber core through a dichroic mirror and a focusing lens, and propagated through the fiber to its tip. Fluorescence signal from excited particles is collected and guided backward through the fiber core, transmitted through the dichroic mirror and filters, and detected by a photomultiplier tube (PMT). Unde-

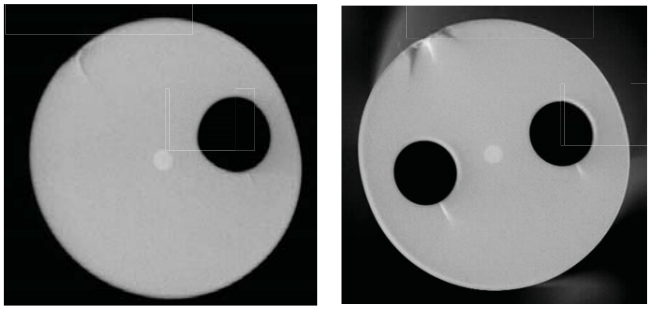

Figure 3.1: Microscope images 125 µm diameter microstructured fibers. The diameter of the holes is ≈ 30 µm.

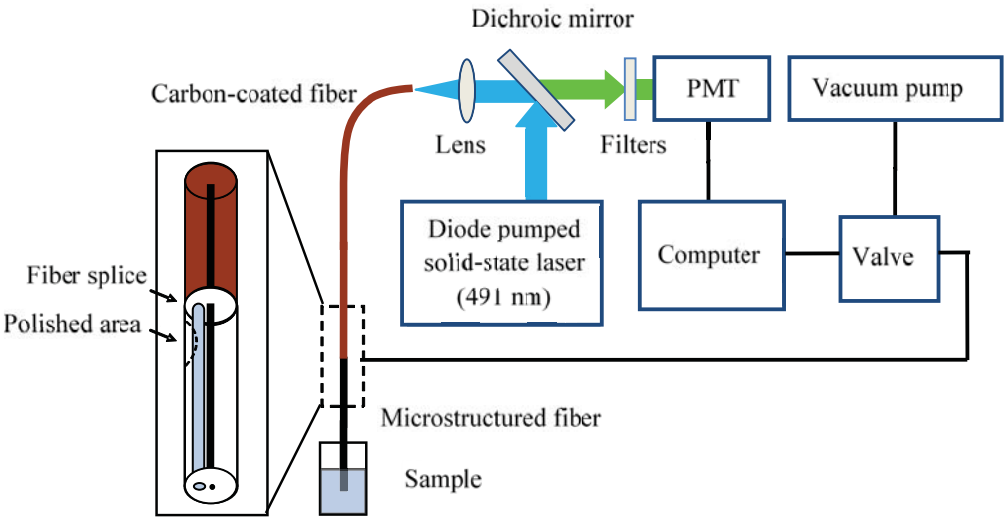

Figure 3.2: Microscope image of a 125 µm diameter microstructured fiber. The diameter of the hole is ≈ 30 µm.

sired light is eliminated using filters placed before the PMT, to ensure that only the fluorescence from the particles is detected.

To allow for liquid flow through the microstructured fiber, one hole is opened from the side by polishing, as schematically shown in Fig. 3.2(a). The polished region is inserted into a needle from the side, through an opening cut in the metal. The needle is coupled to a vacuum pump to enable sample collection in the fiber using under-pressure. A solenoid valve is connected to the vacuum pump to switch on and off the suction of liquid.

When a particle passes near the fiber-core, the PMT signal increases, as shown in Fig. 3.3(a). A signal above a predefined threshold automatically triggers the opening of the valve and, thus, the particle is collected into the hole of the fiber, Fig. 3.3(b). Under typical experimental conditions, the valve is opened for 40 ms and a liquid volume of ≈ 300 pL is sucked into the hole.

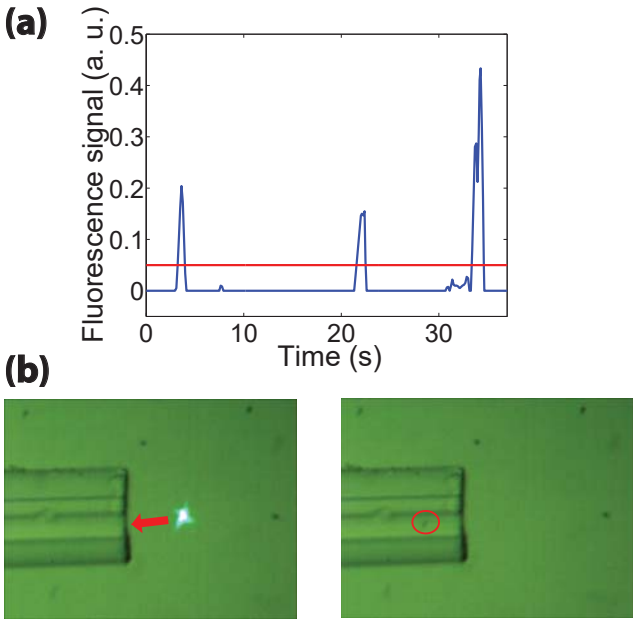

Figure 3.3: (a) Time sequence of the detected signal in the PMT showing that three trigger events take place. (b) Collection of green fluorescent microparticles. (left) The fluorescence signal produced by the particle is detected and activates the trigger that starts the suction mechanism. (right) The particle is retrieved into the hole with the surrounding liquid volume.

Proof-of-principle experiments demonstrate the capabilities of this device, whose potential applications include the in-vivo minimally-invasive monitoring and selective isolation of cells. The fluorescence detection scheme used here could potentially be exchanged or combined with Raman or other scattering detection methods.

3.2 Paper II: Fluidic trapping and optical detection of microparticles with a functional optical fiber

Single-cell manipulation has been widely used for analyzing cell properties and their relation to specific diseases. The realization of in-vivo single-cell trapping and analysis could lead to fast and accurate diagnosis of health disorders, as well as a deeper knowledge about cells in their natural environment.

In **Paper II**, we present a functional fiber probe that can simultaneously trap, excite, and detect fluorescent microparticles in a liquid medium. It integrates particle trapping by micropitte aspiration (Sec. 2.2.1) and light delivery by an optical fiber (Sec. 2.1.2). This device is based on a microstructured optical fiber that has five holes along its cladding and can guide light in a 8 µm central core, Fig. 3.4(a, top), or in the 18 µm area delimited by the holes, Fig. 3.4(a, bottom).

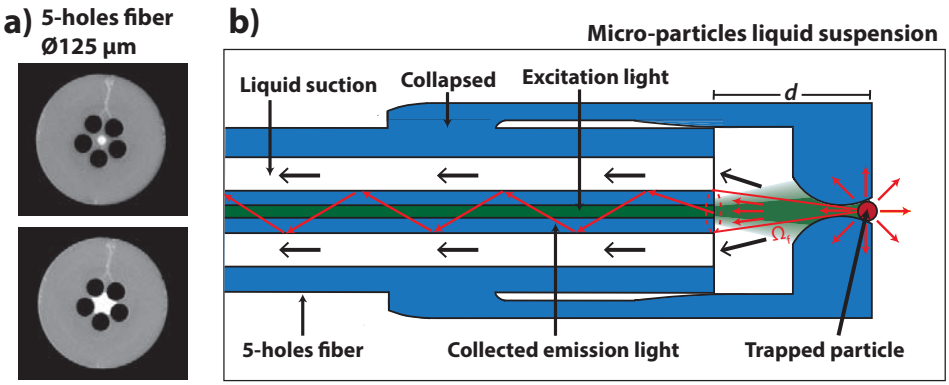

Figure 3.4: Microscope images of the illuminated 5-holes microstructured optical fiber. Laser light is confined in the 8 µm core (top) or in the 18 µm area delimited by the holes (bottom). (b) Schematic of the fiber probe for fluidic trapping and optical detection.

A schematic of the fiber probe is presented in Fig. 3.4(b). The 5-holes fiber is fused to a capillary tip which has an opening smaller than the size of the particle of interest. The probe is immersed in a liquid suspension of fluorescent particles. Differential negative pressure is applied to the remote end of the 5-hole fiber to make the liquid flow into the fiber holes. This causes a suspended particle to be dragged into the opening, where it is trapped. Applying differential positive pressure to the remote end releases the particle. Laser light is coupled to the 8 µm core and travels towards the fiber tip for fluorescence excitation of the particle. Fluorescence emitted by the particle is collected and guided back in the 18 µm waveguiding region towards a detector.

Experimental results are shown in Fig. 3.5. For the probe used here, the capillary tip has an inner diameter of 8 µm. A sufficiently large particle (> 8 µm) blocks

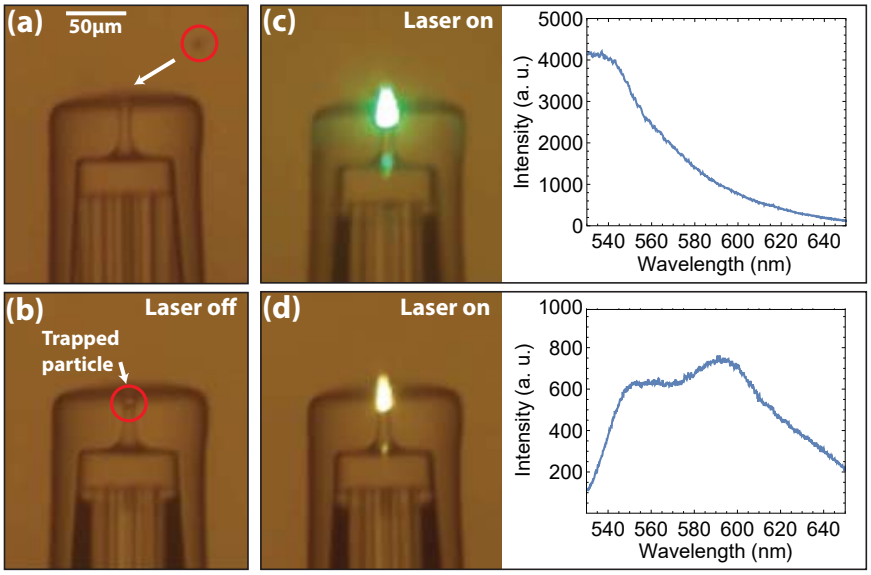

Figure 3.5: Trapping and optical detection of 10 µm fluorescent particles. (a) Particle flowing towards the fiber probe. (b) Particle trapped in the opening of the fiber probe. (c,d) Excitation (left) and recorded spectrum (right) of a green fluorescence particle (c) and a yellow fluorescent particle (d).

the opening and is trapped, as seen in Fig. 3.5(a) and (b). The excitation beam illuminates the trapped particle and its spectrum is measured. Fig. 3.5(c) and (d) show the recorded spectrum of two different types of particles present in the suspension.

The functional fiber probe presented here could be the basis for a system capable of performing an in-vivo and complete characterization of cells.

3.3 Paper III: High performance micro-flow cytometer based on optical fibres

As mention in Sec. 2.3.2, the successful miniaturization and cost reduction of flow cytometers for point-of-care setting is still an open problem. Current micro-flow cytometers do not provide the same performance and number of features than conventional instruments.

In Paper III, we report a micro-flow cytometer entirely based on optical fibers and silica capillaries. The heart of the present system is an integrated micro-chamber where detection of flowing cells takes place. The micro-chamber is built by assembling circular capillaries with a double-clad optical fiber, as illustrated schematically in Fig. 3.6. The detection scheme used in this system was

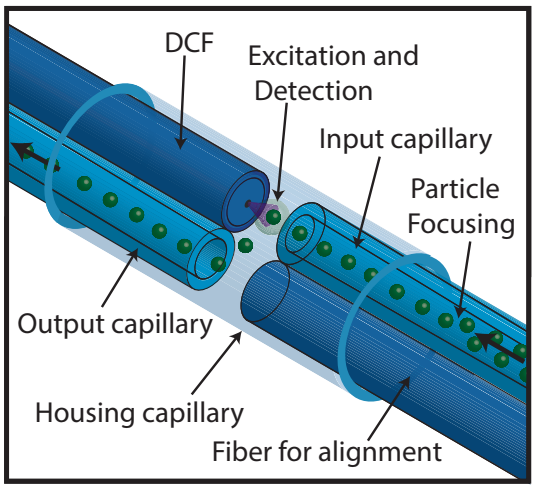

Figure 3.6: Schematic of the fiber microflow cytometer, DCF: double-clad optical fiber.

described in Sec 2.1.2. Laser light propagates in the core of a double-clad fiber (DCF) to the micro-chamber and excites the fluorescent particles or cells delivered by the Input capillary one at a time. Fluorescence and scattering from the particles are collected and guided by the large inner cladding of the same double-clad fiber to the detection system constituted of photomultiplier detectors, dichroic mirrors, and filters. Elasto-inertial microfluidics (Sec 2.9) is used to focus the cells into a single-stream at the center of the Input capillary, guaranteeing accurate and sensitive detection.

As mention in Sec 2.9, **Paper III** presents an complete characeterization of particles focusing in cylindrical capillaries for various Reynolds number, particle size, and capillary diameter. This study enables obtaining the experimental conditions that optimize the focusing of particles and cells. The particle focusing characterization is carried by taking long-exposure fluorescence microscope images of flowing

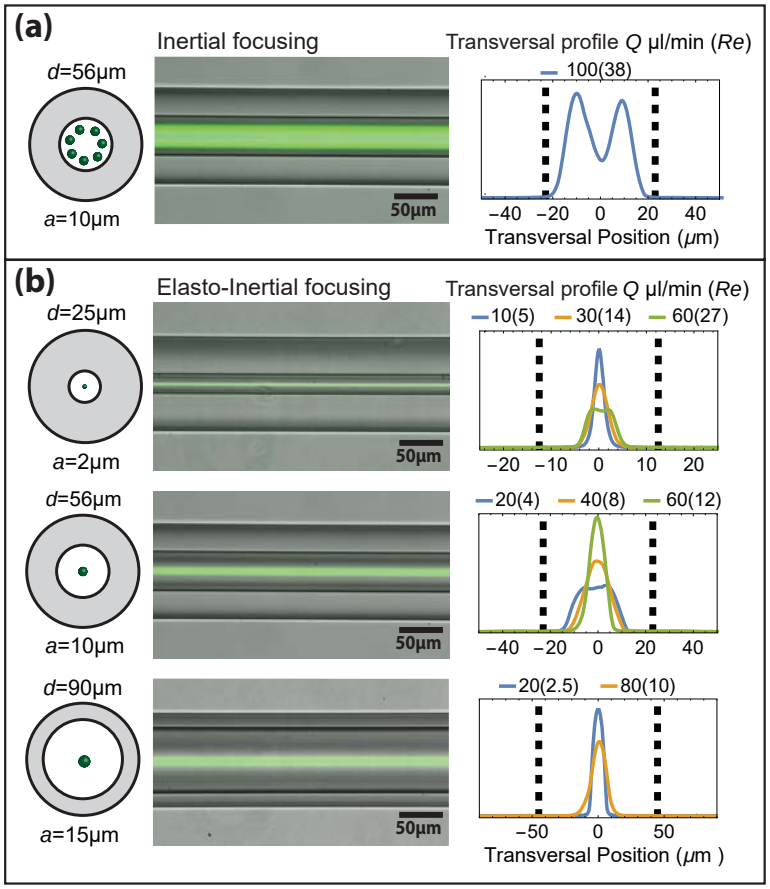

Figure 3.7: Long-exposure fluorescence microscope images and transversal profiles of 10 µm particles focusing in 56 µm cylindrical capillary. (a) Inertial microfluidics. (b) Elasto-inertial microfluidics.

particles. For example, Fig. 3.7(a) corresponds to microscope images of 10 µm focused in a 56 µm by Inertial microfluidics, where particles are suspended in a PBS solution. As expected from Sec 2.4.2, the particles focus in an annulus at ≈ 0.6 times the capillary radius. Elasto-inertial microfluidics, enabled by adding the polymer PEO (elasticity enhancer) to the PBS solution, causes particles to focus into a single-stream at the center of the capillary. This behaviour is shown in Fig. 3.7(b) for 2 µm, 10 µm, and 15 µm particles flowing in 25 µm, 56 µm, 90 µm diameter capillaries, respectively. Focusing is achieved under specific conditions, which depend on the flow rate (Q) and Reynolds number (Re), as indicated by the transversal profiles in Fig. 3.7.

Fig. 3.8(a) shows the effect that single-stream focusing has on particle counting. Green fluorescence particles of 10 µm diameter are injected into the input capillary and flowed to the detection micro-chamber. The input capillary diameter is chosen to be 56 µm, which provides conditions for obtaining both unfocused and focused particle streams depending on the flow rate. Detection of unfocused particles, flowing 25 µL min^{-1}, is shown in Fig. 3.8(a, top). The amplitude of the

fluorescence peaks is non-uniform, presenting a coefficient of variation (CV, ratio between standard deviation and mean) of 88%. Single-stream focusing is achieved by increasing the flow rate to 100 µL min^{-1}, which produces uniform amplitude peaks ($CV = 9\%$), Fig. 3.8(a, bottom). Contrarily to previous studies in Elasto-Inertial microfluidics, here it was found that particle focusing is maintained at high flow rates 800 µL min^{-1}, enabling a throughput of 2500 particle/s.

To demonstrate the versatility of the system, simultaneous detection of two color fluorescence and scattering was carried out with a mixture of 10 µm green fluorescence particles (emission centered at 520 nm) and red fluorescence particles (emission centered at 660 nm) flowed at 100 µL min^{-1}. The wavelength of scattering signal is 450 nm, corresponding to the excitation wavelength of the green fluorescence particles. For example, Fig. 3.8(b) shows a time-slot of 0.4 seconds in a 2 minutes recording of the three signals produced by focused particles. There is a 99% agreement between scattering peaks and the sum of red and green fluorescence peaks.

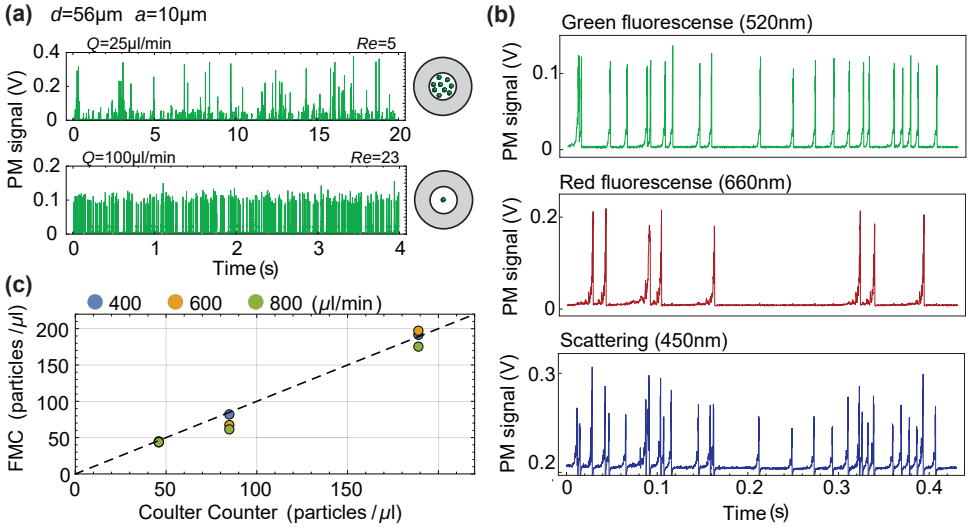

Figure 3.8: Figure 3. (a) Detection of 10 µm fluorescent particles in a 56 µm diameter capillary. Photomultiplier (PM) signal for (top) unfocused particles flowing at 25 µL min^{-1}, and (bottom) focused particles flowing at 100 µL min^{-1}; (b) Detection of scattering and fluorescence from a mixture of green and red 10 µm labelled particles. A total of 8003 green and 2210 red fluorescence particles are detected in 2 minutes, while the scattering events are 10113; (c) Comparison between number of particles measured by the fibre microflow cytometer (FMC) and by Coulter counter for flow rates of 400, 600 and 800 µL min^{-1} and three different concentrations. 15 µm particles are focused in a 90 µm capillary.

The system accuracy is further studied by comparing the number of particles counted with the fiber flow cytometer to measurements performed with a Coulter counter (Beckman coulter, Z2). For this measurement, 15 µm are flowed in a 90 µm capillary. The results of three different particle concentrations, measured in triplicate, flowing at three different flow rates (400, 600 and 800 µL min^{-1}) are shown in

Fig. 3.8(c). The good agreement between the measurements indicates that the fiber microflow cytometer can perform accurate particle counting. Finally, the applicability of the system was tested by analyzing fluorescently labeled cancer cell lines at a high throughput.

The present system is robust, portable (Appendex B), simple and low-cost, solving limitations that have hampered the implementation of flow cytometers at the point of care.

3.4 Paper IV: Microsecond switching of plasmonic nanorods in an all-fiber optofluidic component

Liquid crystal (LC) technology relies on the electrically-induced alignment of anisotropic molecules in a liquid-crystal phase. As described in Sec. 2.5, the response time of liquid crystal devices is limited to milliseconds due to the slow relaxation time of LC molecules when the electric field is turned off. The electrically-induced alignment of plasmonic nanorods suspension has been proposed as a novel paradigm for electro-optical modulation capable of providing much faster response times than LC devices.

In **Paper IV**, we present a compelling study of the dynamics of gold nanorods in suspension when aligned under an electric field, showing response times in the order of microseconds. This study is carried out by using an all-fiber optofluidic device that enables convenient interaction of light, electric fields, and liquid suspensions. The optofluidic component is illustrated in Fig. 3.9. The interaction cell

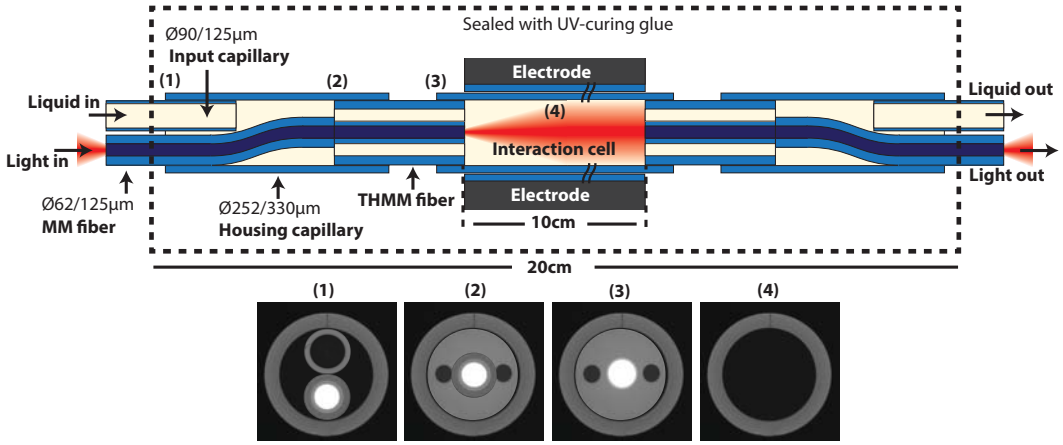

Figure 3.9: Schematic of optofluidic component. Below, photographs of the cross-section at points 1-4. The core region becomes white by coupling light into the remote end of the core

.

where light probes the nanorods consists of a $10\ \mathrm{cm}$ long liquid-core silica capillary with inner/outer diameter $250/330\ \mu\mathrm{m}$. The light is guided by total internal reflection using a solvent (toluene) that has a refractive index higher than silica. The electric field to align the nanorods was created by two electrodes placed on either side of the interaction cell. The electrodes were made by filling similar $250/330\ \mu\mathrm{m}$ capillaries with a low melting temperature alloy 58Bi-42Sn. Light and liquid are delivered to and from the central capillary by using twin-hole multimode fiber (THMM fiber) where the side-holes are used for liquid supply. Optical access to the core of the THMM fiber is provided by a spliced section of standard multimode fiber. The smaller cross-section of this fiber allows splicing without blocking

the holes of the THMM fiber. Liquid delivery is provided by a $90/125$ µm input capillary. The spliced region and a length of the input capillary are introduced into a short (≈ 1 cm) section of housing capillary of diameter $252/330$ µm. This housing capillary is sealed on both sides with UV-curing glue, which prevents liquid from escaping and locks in place the fibers and input capillary. Light coupled to the core of the multimode fiber reaches the interaction cell via the twin-hole fiber. A pressure pump is used to inject liquid into the input capillary, which fills the interaction cell.

The absorbance spectrum for nanorods aligned under an 8 kHz alternating electric fields of different magnitude is shown in Fig. 3.10. Alternating electric field is used to avoid nanorods translation and attachment to the inner walls of the interaction cell. The absorbance is defined as $A = -\log I_0/I$, where I and I_0 are the intensities transmitted through the optofluidic component filled with the nanorod suspension and pure toluene, respectively. These measurements were performed using a white-light source (halogen lamp) and a spectrometer. The polarization of the light is set parallel to the direction of the electric field. The observed behavior agrees with the theoretical description presented in Sec. 2.6.4. When the nanorods align along the electric field direction, the LSPR absorption peak (742 nm) increases, whereas the TSPR peak (532 nm) decreases. Optical parameters such as the plasma frequency and damping constant can be retrieved by fitting the model presented in Sec. 2.6 to the absorbance spectrum for $E = 0$ (black curve, Fig. 3.10). The values obtained are $\omega_p = 14.9 \times 10^{15}$ rad s^{-1} and $\beta = 3.4 \times 10^{14}$ rad s^{-1}.

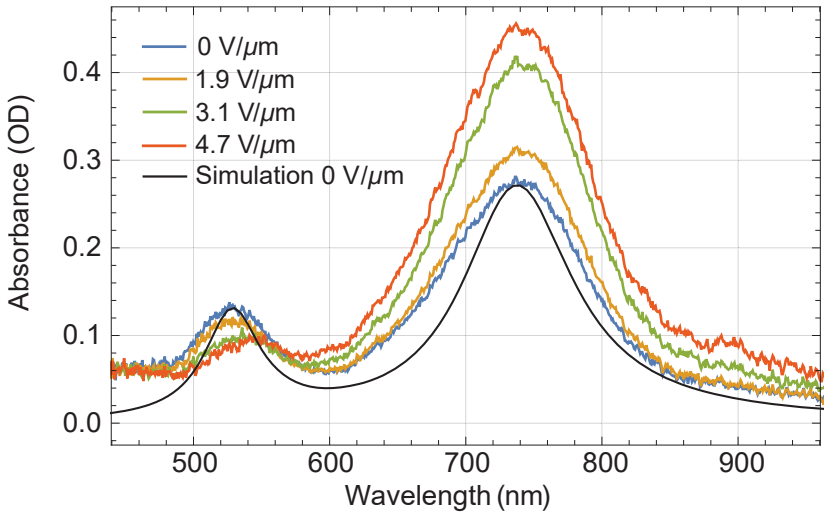

Figure 3.10: Experimental absorbance spectra as a function of wavelength for various applied electric fields (blue–red) and compared to the simulated spectrum at $E = 0$ (black).

Time-resolved measurements were carried out to investigate the dynamics of the system. Fig. 3.11(a) shows the relative absorbance $\Delta A/A_0$ (A_0 is the absorbance for $E = 0$) of the nanorod suspension when appliying a 25 µs rectangular high

voltage pulse that creates an electric field of $9.3\ \mathrm{V\,\mu m^{-1}}$ or $4.1\ \mathrm{V\,\mu m^{-1}}$ in the direction parallel to the light polarization. This measurement was perfomrded using a $690\ \mathrm{nm}$ diode laser and a fast silicon detector. Fitting the theorical model described above allowed obtaining the rotational diffusion coefficent, the anistropy in polarizability, the on-time, and off-time. In this measurement, the retrieved values are $D = 5200\ \mathrm{s^{-1}}$, $\Delta\alpha = 7.5 \times 10^{-}12\ \mathrm{m^3}$, $\tau_{on} = 1.6\ \mu\mathrm{s}$ for $9.3\ \mathrm{V\,\mu m^{-1}}$, and $\tau_{off} = 33\ \mu\mathrm{s}$. The reason of the difference between the experimental value of D and the theoretical value $11200\ \mathrm{s^{-1}}$ (Sec. 2.6.5) is due to the polymer coating of the nanorods, whose effect in the dynamics of the system is experimentally addressed in **Paper IV**. Fig. 3.11(b) shows the on-time as a function of the applied electric field. Times

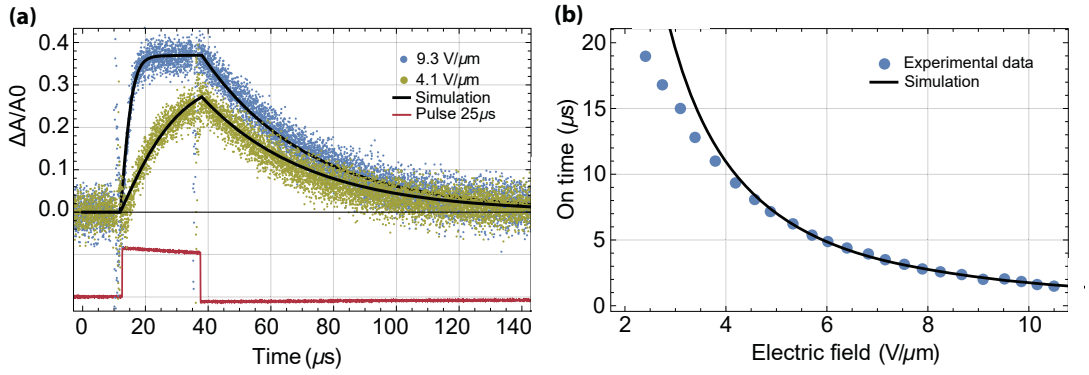

Figure 3.11: Relative absorbance of nanorods aligned under a rectangular pulse signal (red). (a) Pulse of $25\ \mu\mathrm{s}$ width with an electric field $9.3\ \mathrm{V\,\mu m^{-1}}$ (blue) and $4.1\ \mathrm{V\,\mu m^{-1}}$ (green). The simulation (black line) is obtained from the theoretical model described above. (b) On-time as a function of the electric field. Eq. 2.51 has been fitted to the model (black line).

from 18.7 to $1.49\ \mu\mathrm{s}$ are obtained for electric fields from 2.3 to $10.5\ \mathrm{V\,\mu m^{-1}}$. The black line corresponds to a fit of Eq. 2.51, which, as mentioned in Sec. 2.6.5, is valid for strong electric fields. It is possible to see that this equation accuarately describes the experimental data for $> 4\ \mathrm{V\,\mu m^{-1}}$.

In **Paper IV**, the dynamic response is studied in detail for rectangular pulses of different magnitudes and alternating electric fields of different frequencies. This work paves the way towards the use of nanorod suspensions in optical components such as modulators, optical switches or polarization controllers.

3.5 Paper V: Digital electric field induced switching of plasmonic nanorods using an electro-optic fluid fiber

The work presented in **Paper IV** shows that electrical switching of nanorod suspensions can be achieved in microseconds times, offering a much better performance than traditional liquid crystals devices. The limit of microseconds comes from the decay time of nanorods when the electric field switches off (off-time), which is governed by rotational Brownian motion. **Paper V** presents a scheme that could potentially enable nanosecond switching times. In Sec. 2.6.4, the optical response of nanorods when aligned in two orthogonal states, parallel and perpendicular to the light polarization, is simulated (Fig. 2.18). The on-time of the nanorods alignment can be arbitrarily reduced by increasing the electric field applied. Therefore, if the nanorods are digitally switched between these two orthogonal states, then thermal relaxation can be circumvented and the overall response time (on-time and off-time) would be controllable by the magnitude of the applied electric field.

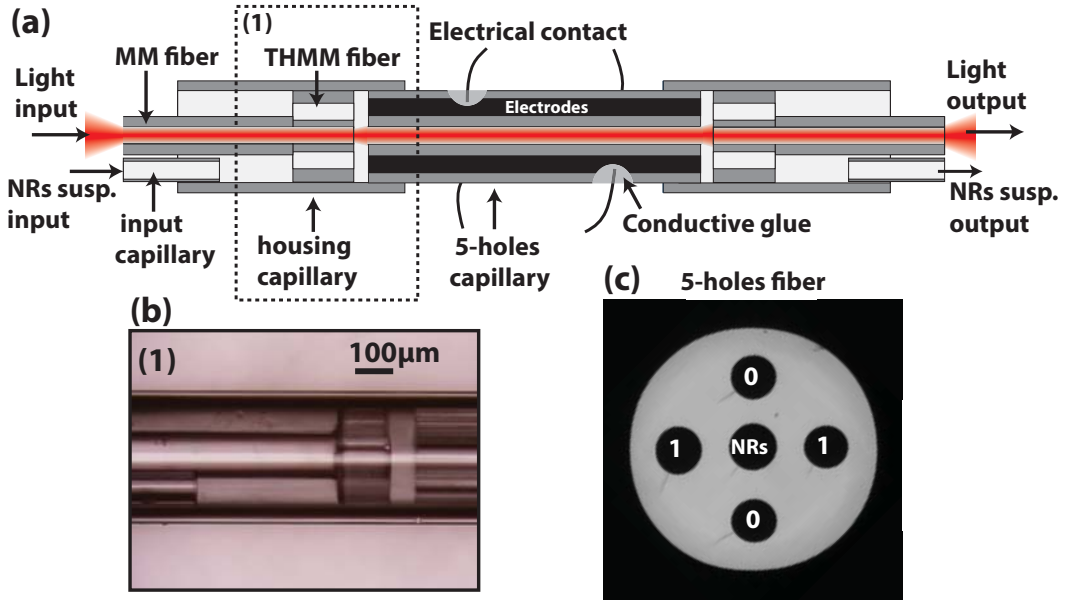

Figure 3.12: (a) Schematic of the fiber component. (b) Microscope image of the part (1) of the fiber component. (c) Microscope image of the 5-hole fiber.

Proof-of-principle experiments of this scheme were performed using the all-fiber optofluidic component shown in Fig. 3.12(a) and (b). This component is similar to the one presented in **Paper IV**, but here the interaction cell consists of a 5-holes fiber, Fig. 3.12(c), which has the four outer $50\ \mu m$ diameter holes filled with metal (BiSn). The metal-filled holes serve as orthogonal digital pairs of electrodes

(channel 0 and channel 1). The procedures for filling the fiber with metal and making electrical contacts for the electrodes are described in Appendix A.2.

Time-resolved switching of the nanorods is presented in Fig 3.13. This measurement was performed using a $730\ nm$ laser and a fast silicon detector. The light was linearly polarized parallel to the 0 channel. Two synchronized high voltage (HV) switches were used to toggle a $200\ \mathrm{kHz}\ 2\ \mathrm{kV}$ driving signal in each channel ($0-$blue/$1-$red) *on* and *off*. The channels were triggered with a $0.6\ \mathrm{ms}$ period square wave, Fig 3.13(black curve). The driving signal is applied to channel 0 when the trigger is high and to channel 1 when the trigger is low.

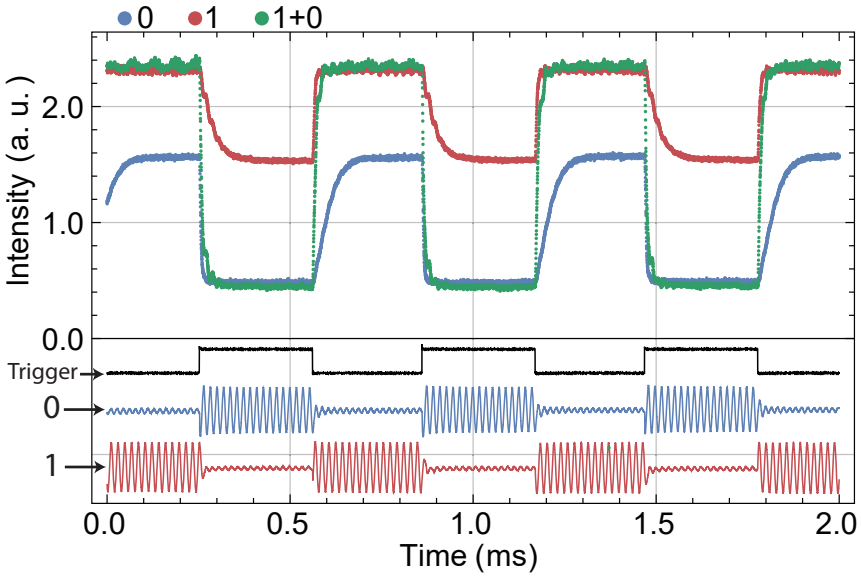

Figure 3.13: Time-resolved digital nanorod switching. Intensity evolution for channel $0-$blue, $1-$red and green $1+0$. The high voltage trigger is shown in black and corresponding driving signals for each channel below, $\omega = 200\ kHz$, $E = 14.8\ V/\mu m$ (channel 0) and $13.5\ V/\mu m$ (channel 1)

The blue curve in Fig 3.13 shows the response as just channel 0 is switched *on* and *off*. With the channel *on* the nanorods quickly align, leading to a decrease in the transmittance at $730\ nm$. When channel 0 is switched *off*, the nanorods begin to randomize due to the thermal rotational diffusion, increasing the transmittance. In contrast, if just channel 1 is switched on, then the transmittance rapidly increases (red curve) and decays to the randomized intensity when channel 1 switches *off*. The period of the driving signal $(5\ \mu s)$ was set to be faster than the thermal relaxation time of the nanorods, therefore, nanorods exposed to the electric field do not have time to thermally decay per AC cycle.

If the driving signal is toggled between channels 0 and 1, then Fig 3.13(green curve) shows the digital response of the nanorods, switching between the 0 and 1 aligned states, thereby demonstrating the removal of the thermal rotation diffusion constraint from the switching mechanism. By fitting an exponential function to the

leading or falling edge of the signals and retrieving the $1/e$ values, the *on*- and *off*-times are defined. The digital *on*- and *off*-times in Fig. 3.13 (green curve) are both 8 μs, at least three times faster than thermal mediated diffusion, and is limited only by the internal response time of the HV switch and driving frequency.

Additionally, **Paper V** presents spectral measurements for nanorods aligned parallel and perpendicular to the polarization of the light, as well as experimental results for the time response of nanorods aligned under a rectangular electric pulse, showing switching of nanorods in 110 ns from an initial unaligned state.

The result presented in this work open the door for the development of electro-optic modulators with nanosecond response by digitally switching nanorods in suspension between two orthogonal states.

Chapter 4

Conclusions

The work presented in this thesis can divided in three different projects:

Advanced optical fiber probes for in-vivo life science applications: In **Paper I**, we demonstrated an optical fiber-based system that allows for collection of microparticles based on their fluorescence signal. In **Paper II**, we presented a functional fiber probe that allows trapping microparticles and measuring their optical signal. Both systems were based on microstructured optical fibers with holes along the cladding, which provide the possibility of exerting fluidic forces on the particles. Future work would be to demonstrate the applicability of the fiber probes for in-vivo studies by testing them with biological particles. Additionally, label-free detection methods, such as Raman scattering, deformability measurements or auto-fluorescence, must be incorporated into these systems to perform cell analysis inside living organisms. This implementation could be readily done in the fiber probe described in **Paper II**, since particle trapping offers the possibility of long detection times and fluidic forces enable stretching cells to characterize their deformability.

Micro-flow cytometer for point-of-care applications: In **Paper III** we presented a high-performance micro-flow cytometer capable of measuring scattering and two-color fluorescence at a throughput of 2500 particles/s. The system was built by combining optical fibers and capillaries, exploiting the intrinsic advantages silica without the need of clean-room facilities or expensive instrumentation. The fact of using cylindrical capillaries for fluid delivery enables focusing of particles or cells into a single stream by Elasto-Inertial microfluidics. This flow cytometer was built into a portable unit (Appendix B) to be used for standard analysis of labeled cells in point of care settings. In spite of the high throughput and accuracy demonstrated, outperforming previous micro-systems, the present device does not provide all the features of modern large-scale flow cytometers. For instance, conventional flow cytometers measure scattering signal at different angles to retrieve information about cell morphology and granularity of its membrane. This could be partially implemented in this fiber system by detecting the light collected by the dummy fiber

used solely for alignment during manufacturing. Nevertheless, a complete scattering analysis would require the incorporation of additional optical fibers placed at different angles, which may be challenging in an integrated all-fiber component. Another direction for future work could be to perform cells sorting based on their fluorescence signal, potentially leading to the development of an all-fiber micro-FACS machine. This implementation could be explored by using microstructured fibers with internal electrodes. In summary, the system described in **Paper III** has the potential to meet the requirements of point-of-care applications and, with further improvements, could result in an alternative to expensive large-scale instruments used in the medical laboratory.

Electrically-induced alignment of gold nanorods: In **Paper IV** we presented a theoretical and experimental study of the dynamics of the electrically-induced alignment of plasmonic gold nanorods in a diluted suspension. The optical response is characterized by using an all-fiber optofluidic component that allows interaction of light, fluids and electric fields. We demonstrated switching times as fast as 1.5 µs when nanorods align to the electric field and 33 µs when nanorods thermally decay to their initial state. Optical and dynamic parameters were obtained by fitting the theoretical model described in Sec. 2.6 to the experimental data. In **Paper V**, we improved the fiber component presented in the previous work by using a microstructured optical fiber with four internal electrodes, which enables digital switching of nanorods between orthogonal aligned states. Experiments indicate that this scheme could allow bidirectional nanosecond switching times, solving the limitation of slow decay times. The results presented in **Paper IV-V** confirm that nanorod suspensions are a viable alternative to liquid crystal devices for electrical modulation of light intensity, providing a faster response time. Future work includes studying the capability of nanorod suspensions to modulate the phase of the light, which could considerably extend the number of possible applications of this system.

To conclude, the three independent projects presented in this thesis and summarized above make use of optical fibers to build optofluidic devices, either single-ended fiber probes that integrate fluidics by using a microstructured fibers or components composed of several fibers and capillaries for optical detection and fluid delivery. This work shows that the all-fiber optofluidic platform, which is an unexplored technology compared to planar microchips, is capable of providing advanced components for distinct applications and can be an alternative to lab-on-a-chip when designing a new system.

Appendix A

Fiber components fabrication

This section describes the instruments and techniques used for manufacturing the all-fiber components presented in **Paper I-V**.

A.1 Vytran GPX-3000

Processing of optical fiber and capillaries was carried out by using a Vytran GPX-3000 station, Fig. A.1. This machine has two positioners that hold one optical fiber each. The positioners enable translational and rotational alignment. A camera, an objective lens, and a system of mirrors provide visualization of lateral and front views of the fibers. Upon starting a process, a tungsten filament supplies the fiber ends with localized heat, enabling fusion splicing. Fiber fusion splicing is a standard process in telecommunications that consists on joining two optical fibers end-to-end, Fig. A.2(a). The rotational control, given by the positioners and the front-view imagining, permit splicing specialty optical fibers, such as polarization maintaining fiber or microstructured optical fibers, Fig. A.2(b). Fibers of different diameter and type can be spliced by appropriately setting the fusion parameters. For instance, in Fig. A.2(c) a thin fiber of diameter 25 µm diameter is spliced to a 125 µm microstructured fiber. This type of splice is utilized for manufacturing the liquid-light combiner presented in **Papers II**. In addition to fusion splicing, the Vytran GPX-3000 can perform fiber tapering, which is discussed in **Paper II**. Fiber tapering consists of reducing the diameter of a fiber or capillary by simultaneous pulling and heating it, Fig. A.2(d). This is done by placing a single fiber along the two positioners and gradually moving them apart while heating the fiber. Additionally, fibers can be cleaved accurately at a desired position by using the Vytran Cleaver (LDC 400). In Fig. A.2(e), a 125 µm diameter fiber is spliced to a 250 µm diameter fiber and subsequently cleaved at 100 µm from the splice. This capability was used to make the fiber-tip presented in **Paper II** and the component used in **Paper V**. The flexibility provided by the positioners of the Vytran GPX-3000 can also be exploited to assemble different capillaries and fibers. Fig. A.2(f) shows a

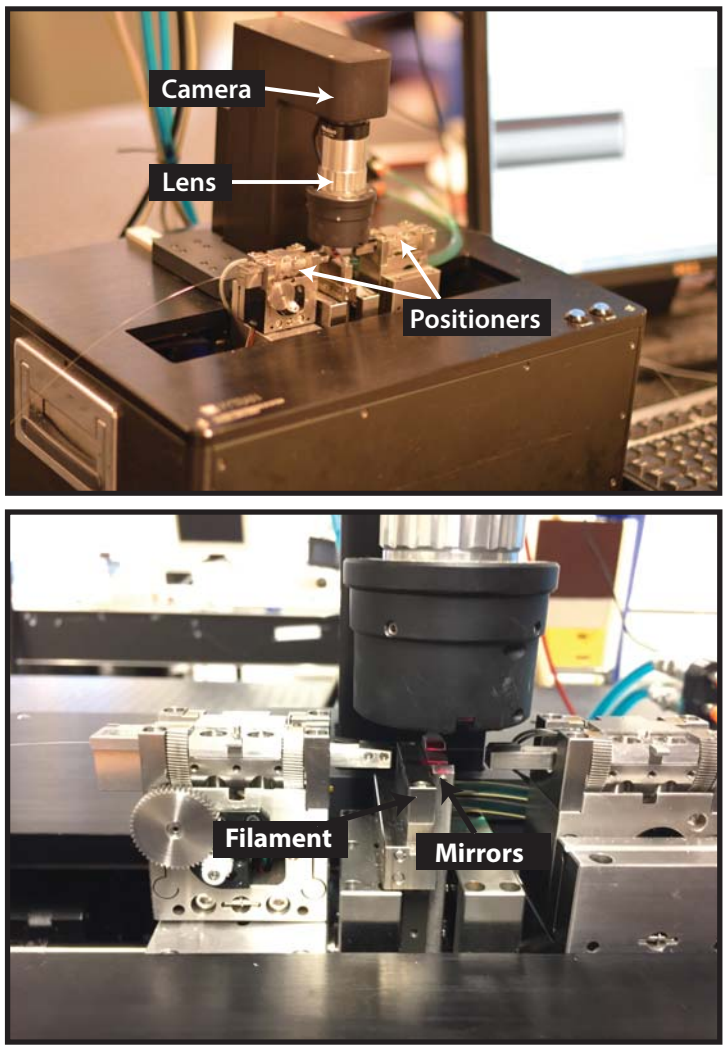

Figure A.1: Vytran GPX 3000

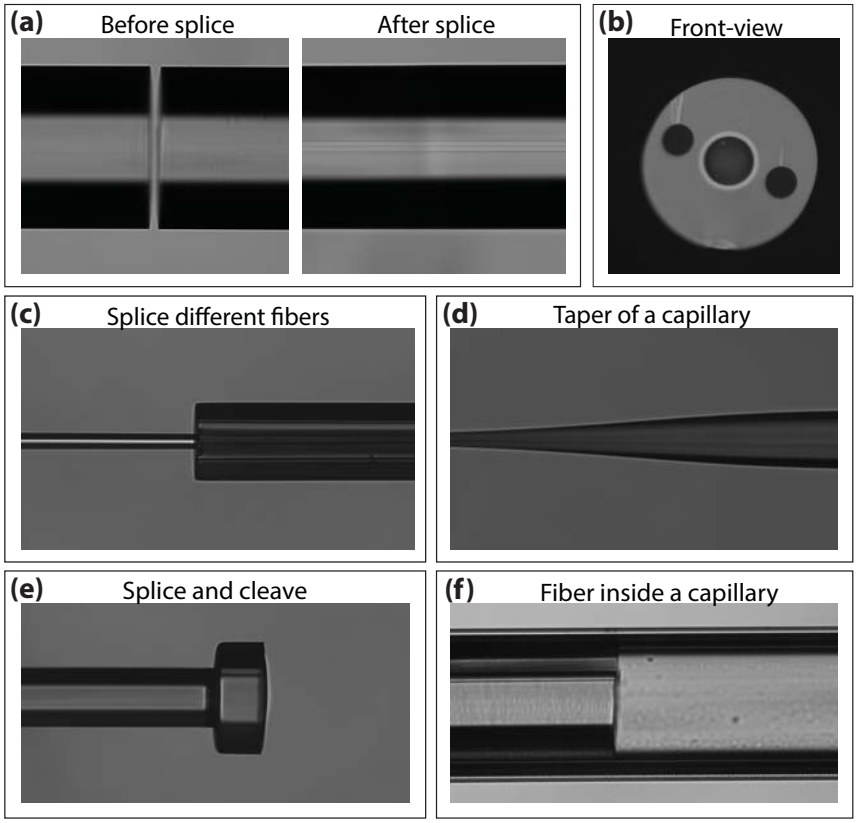

Figure A.2: Vytran GPX 3000 processes. (a) Fusion splice. (b) Front-view of a fiber. (c) Splices of fibers of different type or diameter. (d) Taper of a capillary. (e) Splice and controlled cleaved. (f) Fiber inside a capillary.

fiber inserted in a capillary. The capillary and the fiber are fixed by collapsing the capillary onto the fiber with heat or by gluing them together at the capillary edge. This process was used to fabricate the components described in **Papers III-V**.

A.2 Metal-filled fibers and electrical contacts

The components presented in **Paper IV** and **V** make use of capillaries or microstructured optical fibers that are filled with the metal BiSn. The process of filling fibers with metal is shown schematically in Fig. A.3(a). A container with solid BiSn is placed inside the pressure chamber and both introduced in an oven at $160\ ^{\circ}\mathrm{C}$, which is above the melting-point of BiSn ($137\ ^{\circ}\mathrm{C}$). Once the metal is molten, the chamber is removed from the oven and seven fibers ($420\ \mu\mathrm{m}$ diameter with plastic jacket) are placed inside it, immersed in the liquid metal. The chamber with the fibers is put back inside the oven. The free ends of the fibers are taken outside the oven through an orifice. When the temperature of oven reaches again $160\ ^{\circ}\mathrm{C}$, the chamber is pressurized, and the liquid metal flows into the fiber holes.

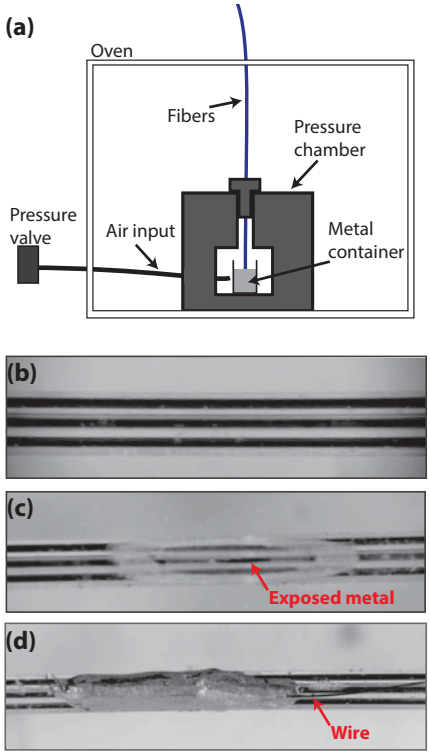

Figure A.3: (a) Schematic of the process for filling fibers with metal. Microscope image of; (b) five-holes fiber with the four outer holes filled with metal (c) Side-polished fiber with exposed metal column, and (d) Electric contact made by silver-based conductive glue.

Finally, the oven is switched off and cools down to room temperature for the metal to solidify. In order to obtain fiber ends free of metal that could be used for splicing, the BiSn columns are shifted by repeating the same process described above, but removing the container with metal from the pressure chamber.

The component used in **Paper V** requires filling the four outer holes of a five-hole fiber with metal, leaving the central hole empty. This is done by splicing a standard telecom fiber of diameter $125\ \mu\mathrm{m}$ to the five-hole fiber before filling it. Since the diameter of the five-hole fiber is $125\ \mu\mathrm{m}$, the central hole is fully blocked by the $125\ \mu\mathrm{m}$ fiber, while the outer holes are only partly blocked and the liquid metal can flow into them. A microscope image of a five-holes fiber with the four outer holes filled with metal is shown in Fig. A.3(b). These metal filled-holes are used as electrodes to apply voltage across the central hole, where the nanorod suspension flows. The electric contacts for these electrodes are made by side-polishing the fiber under a microscope, Fig. A.3(c). Once the electrode is exposed, a copper wire is glued to it by using silver-based conductive glue, as shown in Fig. A.3(d).

Appendix B

Paper III: Portable system

Paper III describes a portable micro-flow cytometer for point-of-care applications. A picture of the complete prototype is shown in Fig. B.1. The optical detection unit, Fig. B.1 (center), was built by assembling components acquired form Thorlabs and Ketek (silicon photomultipliers). The electronics was homebuilt and is described in Appendix C. The photomultipliers gain control and data acquisition were performed by a FPGA unit (Digilent) shown in Fig. B.1(left). The two lasers units, Fig. B.1(right), are composed of pigtailed diode lasers and OEM electronic units, both acquired from Thorlabs.

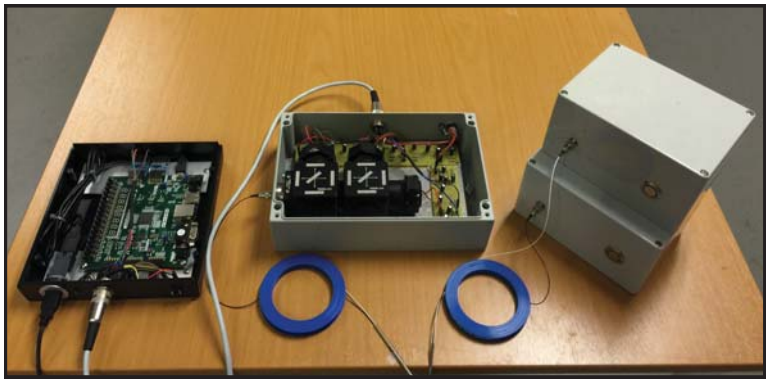

Figure B.1: FPGA control electronics (left), optical detection unit (center), and lasers (right) of the micro-flow cytometer presented in **Paper III**.

Appendix C

Paper III and V: Electronics

The electronic circuit used for controlling and reading the photomultiplier detectors used in the prototype described in **Paper III** is shown Fig. C.1. The circuit provides a regulated output voltage up to $-40\ \mathrm{V}$, from an input of $9\ \mathrm{V}$, to the photomultipliers detectors by using isolated flyback converter. The gain of the detector is set by an analog signal (1-$5\ \mathrm{V}$) from the FPGA. The signal from the detectors is amplified by the circuit and sent to the FPGA for processing. Three of these circuits were built to control and read the three detectors simultaneously.

The electronic circuit for the $2\ \mathrm{kV}\ 200\ \mathrm{kHz}$ AC supplies and the high voltage AC switches used in **Paper V** are shown in Fig. C.2(a) and (b), respectively. The AC supplies correspond to a resonant circuited based on the miniature ferrite transformer 28K077 (T1) acquired from Information unlimited (amazing1.com). The high voltage AC switches consist of a bridge-rectifier and the high voltage power MOSFET IXYS 4500V (Mouser).

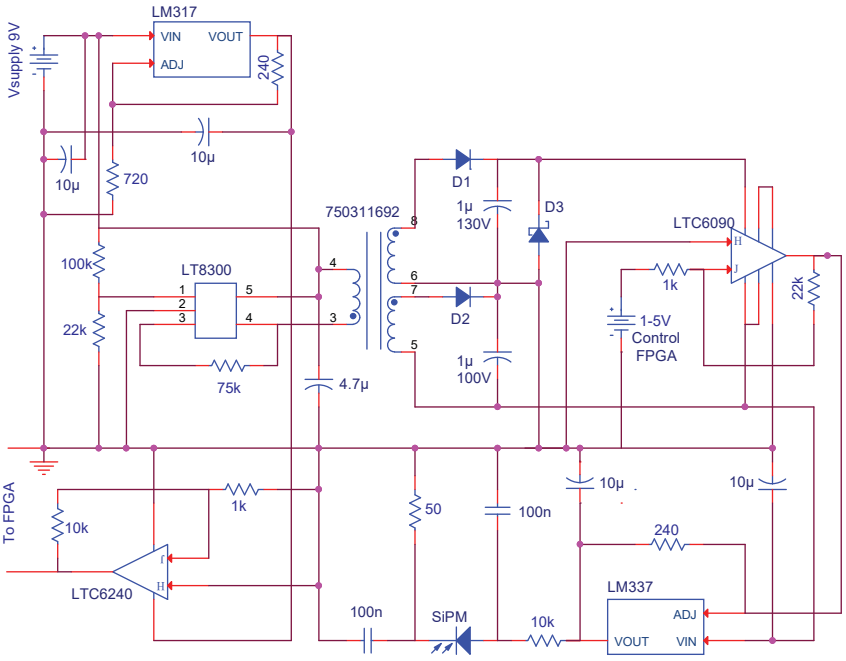

Figure C.1: (a) Electronic circuit for the photomultiplers used in the micro-flow cytometer presented in **Paper III**. D1 and D2: CMMR1U-2-2. D3: CMHZ5266B. SiPM: Silicon photomultiplier (Ketek).

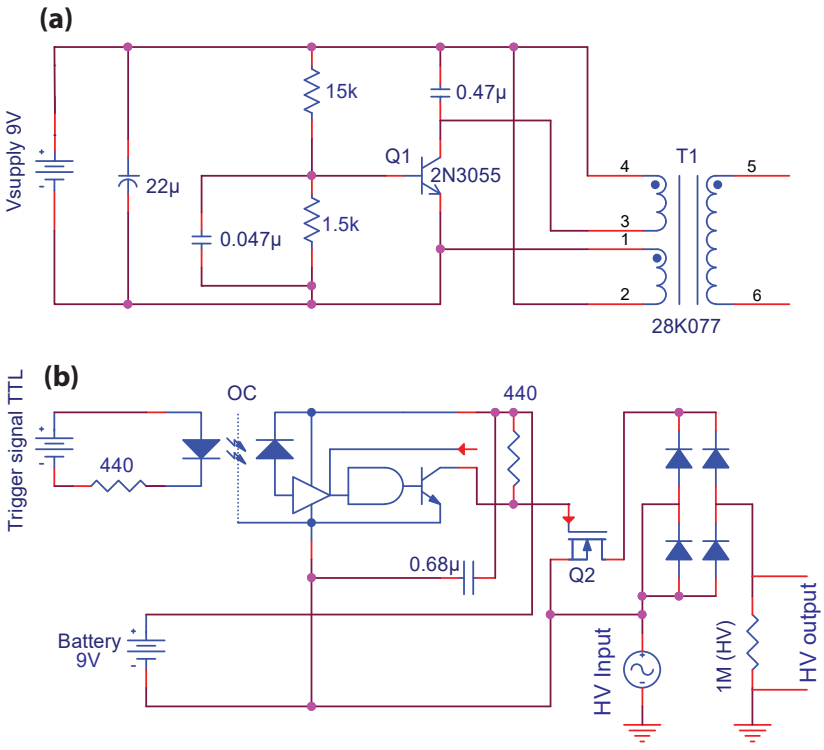

Figure C.2: (a) HV supply 2 kV and 200 kHz. (b) HV switch. OC: opto-coupler. Q2: Mosfet IXYS 4500V. The rectifier diodes used are the DO-41 3000 V.

Bibliography

[1] G. Agrawal, *Fiber-Optic Communication Systems*, 4th ed. Wiley Series in Microwave and Optical Engineering, 2010.

[2] M. C. Teich and B. Saleh, "Fundamentals of photonics", *Canada, Wiley Interscience*, vol. 3, 1991.

[3] J. A. Buck, *Fundamentals of optical fibers*. John Wiley & Sons, 2004.

[4] E. Udd and W. Spillman, *Fiber Optic Sensors: An Introduction for Engineers and Scientists*, 3rd ed. Wiley, 2012.

[5] W. Shi, Q. Fang, X. Zhu, R. A. Norwood, and N. Peyghambarian, "Fiber lasers and their applications [invited]", *Applied Optics*, vol. 53, pp. 6554–6568, 2014.

[6] A. Leung, P. M. Shankar, and R. Mutharasan, "A review of fiber-optic biosensors", *Sensors and Actuators B: Chemical*, vol. 125, no. 2, pp. 688–703, 2007.

[7] G. B. Hocker, "Fiber-optic sensing of pressure and temperature", *Applied Optics*, vol. 18, no. 9, pp. 1445–1448, 1979.

[8] D. J. Richardson, J. Nilsson, and W. A. Clarkson, "High power fiber lasers: Current status and future perspectives [invited]", *Journal of the Optical Society of America B*, vol. 27, B63–B92, 2010.

[9] M. J. F. Digonnet, *Rare-Earth-Doped Fiber Lasers and Amplifiers, Revised and Expanded*. CRC Press, 2001.

[10] H. Dawkins, A. C. Gelijns, N. Rosenberg, and Institute of Medicine, "From the scalpel to the scope: Endoscopic innovations in gastroenterology, gynecology, and surgery", in *Sources of Medical Technology: Universities and Industry*, National Academies Press, 2000, pp. 67–96.

[11] S. A. Boppart, T. F. Deutsch, and D. W. Rattner, "Optical imaging technology in minimally invasive surgery. current status and future directions", *Surgical endoscopy*, vol. 13, no. 5035, pp. 718–722, 1999.

[12] D. Huang, E. A. Swanson, C. P. Lin, J. S. Schuman, W. G. Stinson, W. Chang, M. R. Hee, T. Flotte, K. Gregory, C. A. Puliafito, and J. G. Fujimoto, "Optical coherence tomography", *Science*, vol. 254, no. 5035, pp. 1178–1181, 1991.

[13] B. J. Eggleton, C. Kerbage, P. S. Westbrook, R. S. Windeler, and A. Hale, "Microstructured optical fiber devices", *Opt. Express*, vol. 9, no. 13, pp. 698–713, 2001.

[14] A. Mendez and T. F. Morse, *Specialty Optical Fibers Handbook*. Academic Press, 2006.

[15] R. Kashyap, "Chapter 12 – poling of glasses and optical fibers", in *Fiber Bragg Gratings*, 2nd ed., Elsevier Science, 2009, pp. 527–596.

[16] P. Russel, "Photonic crystal fibers", *Science*, vol. 299, no. 358, pp. 698–713, 2003.

[17] G. M. Whitesides, "The origins and the future of microfluidics", *Nature*, vol. 442, no. 7101, pp. 368–373, 2006.

[18] W. B. Zimmerman, *Microfluidics: history, theory and applications*. Springer Science & Business Media, 2006, vol. 466.

[19] N. T. Nguyen and S. T. Wereley, *Fundamentals and applications of microfluidics*. Artech House, 2002.

[20] T. M. Squires and S. R. Quake, "Microfluidics: Fluid physics at the nanoliter scale", *Reviews of modern physics*, vol. 77, no. 3, p. 977, 2005.

[21] D. J. Beebe, G. A. Mensing, and G. M. Walker, "Physics and applications of microfluidics in biology", *Annual review of biomedical engineerin*, vol. 4, no. 1, pp. 261–286, 2002.

[22] C.-Y. Lee, C.-L. Chang, Y.-N. Wang, and L.-M. Fu, "Microfluidic mixing: A review", *International Journal of Molecular Sciences*, vol. 12, no. 5, pp. 3263–3287, 2011.

[23] A. A. S. Bhagat, H. Bow, H. W. Hou, S. J. Tan, J. Han, and C. T. Lim, "Microfluidics for cell separation", *Medical & Biological Engineering & Computing*, vol. 48, no. 10, pp. 999–1014, 2010.

[24] J. Nilsson, M. Evander, B. Hammarström, and T. Laurell, "Review of cell and particle trapping in microfluidic systems", *Analytica chimica acta*, vol. 649, no. 2, pp. 141–157, 2009.

[25] D. Psaltis, S. R. Quake, and C. Yang, "Developing optofluidic technology through the fusion of microfluidics and optics", *nature*, vol. 442, no. 7101, p. 381, 2006.

[26] C Monat, P Domachuk, and B. Eggleton, "Integrated optofluidics: A new river of light", *Nature photonics*, vol. 1, no. 2, pp. 106–114, 2007.

[27] Y. Fainman, L. Lee, D. Psaltis, and C. Yang, *Optofluidics: fundamentals, devices, and applications*. McGraw-Hill, Inc., 2009.

[28] D. Psaltis, S. R. Quake, and C. Yang, "Developing optofluidic technology through the fusion of microfluidics and optics", *nature*, vol. 442, no. 7101, p. 381, 2006.

[29] Z. Li and D. Psaltis, "Optofluidic dye lasers", *Microfluidics and Nanofluidics*, vol. 4, no. 1-2, pp. 145–158, 2008.

[30] N.-T. Nguyen, "Micro-optofluidic lenses: A review", *Biomicrofluidics*, vol. 4, no. 3, p. 031 501, 2010.

[31] S. Z. Malynych, A. Tokarev, S. Hudson, G. Chumanov, J. Ballato, and K. G. Kornev, "Magneto-controlled illumination with opto-fluidics", *Journal of Magnetism and Magnetic Materials*, vol. 322, no. 14, pp. 1894–1897, 2010.

[32] X. Heng, D. Erickson, L. R. Baugh, Z. Yaqoob, P. W. Sternberg, D. Psaltis, and C. Yang, "Optofluidic microscopy—a method for implementing a high resolution optical microscope on a chip", *Lab on a Chip*, vol. 6, no. 10, pp. 1274–1276, 2006.

[33] A. H. Yang and D. Erickson, "Optofluidic ring resonator switch for optical particle transport", *Lab on a Chip*, vol. 10, no. 6, pp. 769–774, 2010.

[34] J.-P. Delville, M. R. de Saint Vincent, R. D. Schroll, H. Chraïbi, B. Issenmann, R. Wunenburger, D. Lasseux, W. W. Zhang, and E. Brasselet, "Laser microfluidics: Fluid actuation by light", *Journal of Optics A: Pure and Applied Optics*, vol. 11, no. 3, p. 034 015, 2009.

[35] S.-Y. Teh, R. Lin, L.-H. Hung, and A. P. Lee, "Droplet microfluidics", *Lab on a Chip*, vol. 8, no. 2, pp. 198–220, 2008.

[36] K. E. Herold and A. Rasooly, *Lab on a Chip Technology: Fabrication and microfluidics*. Horizon Scientific Press, 2009, vol. 1.

[37] D. Figeys and D. Pinto, "Lab-on-a-chip: A revolution in biological and medical sciences.", *Analytical Chemistry*, vol. 72, no. 9, 330 A–335 A, 2000.

[38] P. Yager, T. Edwards, E. Fu, K. Helton, K. Nelson, M. R. Tam, and B. H. Weigl, "Microfluidic diagnostic technologies for global public health", *Nature*, vol. 442, no. 7101, p. 412, 2006.

[39] V. Gubala, L. F. Harris, A. J. Ricco, M. X. Tan, and D. E. Williams, "Point of care diagnostics: Status and future", *Analytical chemistry*, vol. 84, no. 2, pp. 487–515, 2011.

[40] S. A. Maier, *Plasmonics: fundamentals and applications*. Springer Science & Business Media, 2007.

[41] K. A. Willets and R. P. Van Duyne, "Localized surface plasmon resonance spectroscopy and sensing", *Annu. Rev. Phys. Chem.*, vol. 58, pp. 267–297, 2007.

[42] C. Noguez, "Surface plasmons on metal nanoparticles: The influence of shape and physical environment", *The Journal of Physical Chemistry C*, vol. 111, no. 10, pp. 3806–3819, 2007.

[43] J. Zhao, X. Zhang, C. R. Yonzon, A. J. Haes, and R. P. Van Duyne, "Localized surface plasmon resonance biosensors", *Nanomedicine*, vol. 1, no. 2, pp. 219–228, 2006.

[44] K. Kneipp, Y. Wang, H. Kneipp, L. T. Perelman, I. Itzkan, R. R. Dasari, and M. S. Feld, "Single molecule detection using surface-enhanced raman scattering (sers)", *Physical review letters*, vol. 78, no. 9, p. 1667, 1997.

[45] A. Cusano, M. Consales, A. Crescitelli, and A. Ricciardi, *Lab-on-fiber technology*. Springer, 2015, vol. 56.

[46] P. Vaiano, B. Carotenuto, M. Pisco, A. Ricciardi, G. Quero, M. Consales, A. Crescitelli, E. Esposito, and A. Cusano, "Lab on fiber technology for biological sensing applications", *Laser & Photonics Reviews*, vol. 10, no. 6, pp. 922–961, 2016.

[47] D. L. Stokes and T. Vo-Dinh, "Development of an integrated single-fiber sers sensor", *Sensors and Actuators B: Chemical*, vol. 69, no. 1, pp. 28–36, 2000.

[48] X. Ma, H. Huo, W. Wang, Y. Tian, N. Wu, C. Guthy, M. Shen, and X. Wang, "Surface-enhanced raman scattering sensor on an optical fiber probe fabricated with a femtosecond laser", *Sensors*, vol. 10, no. 12, pp. 11 064–11 071, 2010.

[49] M. Islam, X. Zhao, A. Said, S. Mickel, and C. Vail, "High-efficiency and high-resolution fiber-optic probes for near field imaging and spectroscopy", *Applied physics letters*, vol. 71, no. 20, pp. 2886–2888, 1997.

[50] Z. Liu, C. Guo, J. Yang, and L. Yuan, "Tapered fiber optical tweezers for microscopic particle trapping: Fabrication and application", *Optics express*, vol. 14, no. 25, pp. 12 510–12 516, 2006.

[51] C. Liberale, P. Minzioni, F. Bragheri, F. De Angelis, E. Di Fabrizio, and I. Cristiani, "Miniaturized all-fibre probe for three-dimensional optical trapping and manipulation", *Nature photonics*, vol. 1, no. 12, pp. 723–727, 2007.

[52] N. Saucedo-Zeni, S. Mewes, R. Niestroj, L. Gasiorowski, D. Murawa, P. Nowaczyk, T. Tomasi, E. Weber, G. Dworacki, N. G. Morgenthaler, *et al.*, "A novel method for the in vivo isolation of circulating tumor cells from peripheral blood of cancer patients using a functionalized and structured medical wire", *International journal of oncology*, vol. 41, no. 4, pp. 1241–1250, 2012.

[53] J. C. McDonald, D. C. Duffy, J. R. Anderson, D. T. Chiu, H. Wu, O. J. A. Schueller, and G. M. Whitesides, "Fabrication of microfluidic systems in poly(dimethylsiloxane)", *ELECTROPHORESIS*, vol. 21, no. 1, pp. 27–40, 2000.

[54] S. K. Sia and G. M. Whitesides, "Microfluidic devices fabricated in poly (dimethylsiloxane) for biological studies", *Electrophoresis*, vol. 24, no. 21, pp. 3563–3576, 2003.

[55] B. S. Hardy, K. Uechi, J. Zhen, and H. Pirouz Kavehpour, "The deformation of flexible pdms microchannels under a pressure driven flow", *Lab Chip*, vol. 9, no. 7, pp. 935–938, 2009.

[56] T. C. Merkel, V. I. Bondar, K. Nagai, B. D. Freeman, and I. Pinnau, "Gas sorption, diffusion, and permeation in poly(dimethylsiloxane)", *Journal of Polymer Science Part B: Polymer Physics*, vol. 38, no. 3, pp. 415–434, 2000.

[57] R. Mukhopadhyay, "When pdms isn't the best", *Analytical Chemistry*, vol. 79, no. 9, pp. 3248–3253, 2007.

[58] N. P. Bansal and R. H. Doremus, *Handbook of glass properties*. Elsevier, 2013.

[59] B. Renberg, K. Sato, T. Tsukahara, K. Mawatari, and T. Kitamori, "Hands on: Thermal bonding of nano- and microfluidic chips", *Microchimica Acta*, vol. 166, no. 1, pp. 177–181, 2009.

[60] T. Li, *Optical fiber communications: fiber fabrication*. Elsevier, 2012.

[61] A. Sudirman and W. Margulis, "All-fiber optofluidic component to combine light and fluid", *IEEE Photon. Technol. Lett.*, vol. 26, pp. 1031–1033, 2014.

[62] R. M. Gerosa, A. Sudirman, L. d. S. Menezes, W. Margulis, and C. J. de Matos, "All-fiber high repetition rate microfluidic dye laser", *Optica*, vol. 2, no. 2, pp. 186–193, 2015.

[63] M Vieweg, T Gissibl, S Pricking, B. Kuhlmey, D. Wu, B. Eggleton, and H Giessen, "Ultrafast nonlinear optofluidics in selectively liquid-filled photonic crystal fibers", *Optics express*, vol. 18, no. 24, pp. 25 232–25 240, 2010.

[64] H. Zhang, S. Chang, J. Yuan, and D. Huang, "Supercontinuum generation in chloroform-filled photonic crystal fibers", *Optik-International Journal for Light and Electron Optics*, vol. 121, no. 9, pp. 783–787, 2010.

[65] M. Calcerrada, C. García-Ruiz, and M. González-Herráez, "Chemical and biochemical sensing applications of microstructured optical fiber-based systems", *Laser & Photonics Reviews*, vol. 9, no. 6, pp. 604–627, 2015.

[66] H. Lehmann, S. Brueckner, J. Kobelke, G. Schwotzer, K. Schuster, and R. Willsch, "Toward photonic crystal fiber based distributed chemosensors", in *Proc. SPIE*, vol. 5855, 2005, pp. 419–422.

[67] M. Brown and C. Wittwer, "Flow cytometry: Principles and clinical applications in hematology", *Clinical chemistry*, vol. 46, no. 8, pp. 1221–1229, 2000.

[68] A. Adan, G. Alizada, Y. Kiraz, Y. Baran, and A. Nalbant, "Flow cytometry: Basic principles and applications", *Critical reviews in biotechnology*, vol. 37, no. 2, pp. 163–176, 2017.

[69] C. J. Engelbrecht, W. Göbel, and F. Helmchen, "Enhanced fluorescence signal in nonlinear microscopy through supplementary fiber-optic light collection", *Opt. Express*, vol. 17, no. 8, pp. 6421–6435, 2009.

[70] G. Bao and S. Suresh, "Cell and molecular mechanics of biological materials", *Nature materials*, vol. 2, no. 11, p. 715, 2003.

[71] A. Ashkin, J. M. Dziedzic, J. Bjorkholm, and S. Chu, "Observation of a single-beam gradient force optical trap for dielectric particles", *Optics letters*, vol. 11, no. 5, pp. 288–290, 1986.

[72] R. M. Hochmuth, "Micropipette aspiration of living cells", *Journal of biomechanics*, vol. 33, no. 1, pp. 15–22, 2000.

[73] Z. Ulanowski, "Optical tweezers-principles and applications", in *Proc. Roy. Microsc. Soc*, 2001.

[74] A. Ashkin and J. M. Dziedzic, "Optical trapping and manipulation of viruses and bacteria", *Science*, vol. 235, pp. 1517–1521, 1987.

[75] L. Wilson, P. T. Matsudaira, and M. P. Sheetz, *Laser tweezers in cell biology*. Academic Press, 1997, vol. 55.

[76] H. Zhang and K.-K. Liu, "Optical tweezers for single cells", *Journal of The Royal Society Interface*, vol. 5, no. 24, pp. 671–690, 2008.

[77] K. C. Neuman and A. Nagy, "Single-molecule force spectroscopy: Optical tweezers, magnetic tweezers and atomic force microscopy", *Nature methods*, vol. 5, no. 6, pp. 491–505, 2008.

[78] D. G. Grier, "A revolution in optical manipulation", *nature*, vol. 424, no. 6950, p. 810, 2003.

[79] S. Chien, "Red cell deformability and its relevance to blood flow", *Annual review of physiology*, vol. 49, no. 1, pp. 177–192, 1987.

[80] C. Bustamante, Z. Bryant, and S. B. Smith, "Ten years of tension: Single-molecule dna mechanics", *Nature*, vol. 421, no. 6921, pp. 423–427, 2003.

[81] E. Harlow, D. Lane, *et al.*, "A laboratory manual", *New York: Cold Spring Harbor Laboratory*, vol. 579, 1988.

[82] D. A. Basiji, W. E. Ortyn, L. Liang, V. Venkatachalam, and P. Morrissey, "Cellular image analysis and imaging by flow cytometry", *Clinics in laboratory medicine*, vol. 27, no. 3, pp. 653–670, 2007.

[83] T. Sun and H. Morgan, "Single-cell microfluidic impedance cytometry: A review", *Microfluidics and Nanofluidics*, vol. 8, no. 4, pp. 423–443, 2010.

[84] M. Ward, P. Turner, M. DeJohn, and G. Kaduchak, "Fundamentals of acoustic cytometry", *Current Protocols in Cytometry*, pp. 1–22, 2009.

[85] W. Bonner, H. Hulett, R. Sweet, and L. Herzenberg, "Fluorescence activated cell sorting", *Review of Scientific Instruments*, vol. 43, no. 3, pp. 404–409, 1972.

[86] D. A. Watson, L. O. Brown, D. F. Gaskill, M. Naivar, S. W. Graves, S. K. Doorn, and J. P. Nolan, "A flow cytometer for the measurement of raman spectra", *Cytometry Part A*, vol. 73, no. 2, pp. 119–128, 2008.

[87] O. Otto, P. Rosendahl, A. Mietke, S. Golfier, C. Herold, D. Klaue, S. Girardo, S. Pagliara, A. Ekpenyong, A. Jacobi, *et al.*, "Real-time deformability cytometry: On-the-fly cell mechanical phenotyping", *Nature methods*, vol. 12, no. 3, pp. 199–202, 2015.

[88] D. A. Ateya, J. S. Erickson, P. B. Howell, L. R. Hilliard, J. P. Golden, and F. S. Ligler, "The good, the bad, and the tiny: A review of microflow cytometry", *Analytical and bioanalytical chemistry*, vol. 391, no. 5, pp. 1485–1498, 2008.

[89] D. Huh, W. Gu, Y. Kamotani, J. B. Grotberg, and S. Takayama, "Microfluidics for flow cytometric analysis of cells and particles", *Physiological measurement*, vol. 26, no. 3, R73, 2005.

[90] D. Schafer, E. A. Gibson, E. A. Salim, A. E. Palmer, R. Jimenez, and J. Squier, "Microfluidic cell counter with embedded optical fibers fabricated by femtosecond laser ablation and anodic bonding", *Optics express*, vol. 17, no. 8, pp. 6068–6073, 2009.

[91] J. P. Golden, J. S. Kim, J. S. Erickson, L. R. Hilliard, P. B. Howell, G. P. Anderson, M. Nasir, and F. S. Ligler, "Multi-wavelength microflow cytometer using groove-generated sheath flow", *Lab on a Chip*, vol. 9, no. 13, pp. 1942–1950, 2009.

[92] J. Godin and Y.-H. Lo, "Two-parameter angular light scatter collection for microfluidic flow cytometry by unique waveguide structures", *Biomedical optics express*, vol. 1, no. 5, pp. 1472–1479, 2010.

[93] J. D. Anderson and J Wendt, *Computational fluid dynamics*. Springer, 1995, vol. 206.

[94] E. S. Asmolov, "The inertial lift on a spherical particle in a plane poiseuille flow at large channel reynolds number", *Journal of Fluid Mechanics*, vol. 381, pp. 63–87, 1999.

[95] D. Di Carlo, "Inertial microfluidics", *Lab on a Chip*, vol. 9, no. 21, pp. 3038–3046, 2009.

[96] J. Zhang, S. Yan, D. Yuan, G. Alici, N.-T. Nguyen, M. Ebrahimi Warkiani, and W. Li, "Fundamentals and applications of inertial microfluidics: A review", *Lab on a Chip*, vol. 16, no. 1, pp. 10–34, 2015.

[97] J. M. Martel and M. Toner, "Inertial focusing in microfluidics", *Annual Review of Biomedical Engineering*, vol. 16, pp. 371–396,

[98] G Segre, "Radial particle displacements in poiseuille flow of suspensions", *Nature*, vol. 189, pp. 209–210, 1961.

[99] S. Ookawara, D. Street, and K. Ogawa, "Numerical study on development of particle concentration profiles in a curved microchannel", *Chemical engineering science*, vol. 61, no. 11, pp. 3714–3724, 2006.

[100] A. A. S. Bhagat, H. W. Hou, L. D. Li, C. T. Lim, and J. Han, "Pinched flow coupled shear-modulated inertial microfluidics for high-throughput rare blood cell separation", *Lab on a Chip*, vol. 11, no. 11, pp. 1870–1878, 2011.

[101] D. R. Gossett, W. M. Weaver, A. J. Mach, S. C. Hur, H. T. K. Tse, W. Lee, H. Amini, and D. Di Carlo, "Label-free cell separation and sorting in microfluidic systems", *Analytical and bioanalytical chemistry*, vol. 397, no. 8, pp. 3249–3267, 2010.

[102] S. C. Hur, H. T. K. Tse, and D. Di Carlo, "Sheathless inertial cell ordering for extreme throughput flow cytometry", *Lab on a Chip*, vol. 10, no. 3, pp. 274–280, 2010.

[103] J. Hansson, J. M. Karlsson, T. Haraldsson, H. Brismar, W. van der Wijngaart, and A. Russom, "Inertial microfluidics in parallel channels for high-throughput applications", *Lab on a Chip*, vol. 12, no. 22, pp. 4644–4650, 2012.

[104] A. Leshansky, A Bransky, N Korin, and U Dinnar, "Tunable nonlinear viscoelastic "focusing" in a microfluidic device", *Physical review letters*, vol. 98, no. 23, p. 234 501, 2007.

[105] G. D'Avino, G. Romeo, M. M. Villone, F. Greco, P. A. Netti, and P. L. Maffettone, "Single line particle focusing induced by viscoelasticity of the suspending liquid: Theory, experiments and simulations to design a micropipe flow-focuser", *Lab on a Chip*, vol. 12, no. 9, pp. 1638–1645, 2012.

[106] K. W. Seo, H. J. Byeon, H. K. Huh, and S. J. Lee, "Particle migration and single-line particle focusing in microscale pipe flow of viscoelastic fluids", *RSC Advances*, vol. 4, no. 7, pp. 3512–3520, 2014.

[107] J. Nam, H. Lim, D. Kim, H. Jung, and S. Shin, "Continuous separation of microparticles in a microfluidic channel via the elasto-inertial effect of non-newtonian fluid", *Lab on a Chip*, vol. 12, no. 7, pp. 1347–1354, 2012.

[108] S. Yang, J. Y. Kim, S. J. Lee, S. S. Lee, and J. M. Kim, "Sheathless elasto-inertial particle focusing and continuous separation in a straight rectangular microchannel", *Lab on a Chip*, vol. 11, no. 2, pp. 266–273, 2011.

[109] G. Li, G. H. McKinley, and A. M. Ardekani, "Dynamics of particle migration in channel flow of viscoelastic fluids", *Journal of Fluid Mechanics*, vol. 785, pp. 486–505, 2015.

[110] H. Lim, J. Nam, and S. Shin, "Lateral migration of particles suspended in viscoelastic fluids in a microchannel flow", *Microfluidics and nanofluidics*, vol. 17, no. 4, p. 683, 2014.

[111] N. Xiang, X. Zhang, Q. Dai, J. Cheng, K. Chen, and Z. Ni, "Fundamentals of elasto-inertial particle focusing in curved microfluidic channels", *Lab on a Chip*, vol. 16, no. 14, pp. 2626–2635, 2016.

[112] J. Prost, *The physics of liquid crystals*. Oxford university press, 1995, vol. 83.

[113] V. G. Chigrinov, *Liquid crystal devices: physics and applications*. 1999.

[114] D.-K. Yang, *Fundamentals of liquid crystal devices*. John Wiley & Sons, 2014.

[115] R. H. Chen, *Liquid crystal displays: fundamental physics and technology*. John Wiley & Sons, 2011.

[116] K. Takatoh, M. Sakamoto, R. Hasegawa, M. Koden, N. Itoh, and M. Hasegawa, *Alignment technology and applications of liquid crystal devices*. CRC Press, 2005.

[117] F. M. Leslie, "Continuum theory for nematic liquid crystals", *Continuum Mechanics and Thermodynamics*, vol. 4, no. 3, pp. 167–175, 1992.

[118] J. Aizpurua, G. W. Bryant, L. J. Richter, F. G. De Abajo, B. K. Kelley, and T Mallouk, "Optical properties of coupled metallic nanorods for field-enhanced spectroscopy", *Physical Review B*, vol. 71, no. 23, p. 235 420, 2005.

[119] J. N. Anker, W. P. Hall, O. Lyandres, N. C. Shah, J. Zhao, and R. P. Van Duyne, "Biosensing with plasmonic nanosensors", *Nature materials*, vol. 7, no. 6, pp. 442–453, 2008.

[120] C. J. Murphy, A. M. Gole, J. W. Stone, P. N. Sisco, A. M. Alkilany, E. C. Goldsmith, and S. C. Baxter, "Gold nanoparticles in biology: Beyond toxicity to cellular imaging", *Accounts of chemical research*, vol. 41, no. 12, pp. 1721–1730, 2008.

[121] Y.-Y. Yu, S.-S. Chang, C.-L. Lee, and C. C. Wang, "Gold nanorods: Electrochemical synthesis and optical properties", *The Journal of Physical Chemistry B*, vol. 101, no. 34, pp. 6661–6664, 1997.

[122] M. Quinten, "Chapter 14: Effective medium theories", in *Optical properties of nanoparticle systems: Mie and beyond*, John Wiley & Sons, 2010.

[123] M. Mohammadimasoudi, Z. Hens, and K. Neyts, "Full alignment of dispersed colloidal nanorods by alternating electric fields", *RSC Advances*, vol. 6, no. 61, pp. 55 736–55 744, 2016.

[124] P. Zijlstra, M. van Stee, N. Verhart, Z. Gu, and M. Orrit, "Rotational diffusion and alignment of short gold nanorods in an external electric field", *Physical Chemistry Chemical Physics*, vol. 14, no. 13, pp. 4584–4588, 2012.

[125] E. Nelson, E. Nelson, E. Nelson, and E. Nelson, *Dynamical theories of Brownian motion*. Princeton university press Princeton, 1967, vol. 3.

[126] I. Karatzas and S. Shreve, *Brownian motion and stochastic calculus*. Springer Science & Business Media, 2012, vol. 113.

[127] B. Felderhof and R. Jones, "Nonlinear response of a dipolar system with rotational diffusion to an oscillating field", *Journal of Physics: Condensed Matter*, vol. 15, no. 15, S1363, 2003.

[128] M. Islam, "Einstein–smoluchowski diffusion equation: A discussion", *Physica Scripta*, vol. 70, no. 2-3, p. 120, 2004.

[129] D. B. Reeves and J. B. Weaver, "Simulations of magnetic nanoparticle brownian motion", *Journal of applied physics*, vol. 112, no. 12, p. 124 311, 2012.

[130] A. de La Cotte, P. Merzeau, J. W. Kim, K. Lahlil, J.-P. Boilot, T. Gacoin, and E. Grelet, "Electric field induced birefringence in non-aqueous dispersions of mineral nanorods", *Soft matter*, vol. 11, no. 33, pp. 6595–6603, 2015.

[131] M. M. Tirado, C. L. Martínez, and J. G. de la Torre, "Comparison of theories for the translational and rotational diffusion coefficients of rod-like macromolecules. application to short dna fragments", *The Journal of chemical physics*, vol. 81, no. 4, pp. 2047–2052, 1984.

[132] A. Sudirman, L. Norin, and W. Margulis, "Increased sensitivity in fiber-based spectroscopy using carbon-coated fiber", *Optics express*, vol. 20, no. 27, pp. 28 049–28 055, 2012.

Appendix D

Paper Reprints